Spatiotemporal spread of perturbations in a driven dissipative Duffing chain: An out-of-time-ordered correlator approach

Amit Kumar Chatterjee [ID],[*] Anupam Kundu,[†] and Manas Kulkarni[‡]
International Centre for Theoretical Sciences, Tata Institute of Fundamental Research, Bengaluru 560089, India

Out-of-time-ordered correlators (OTOCs) have been extensively used as a major tool for exploring quantum chaos, and recently there has been a classical analog. Studies have been limited to closed systems. In this work, we probe an open classical many-body system, more specifically, a spatially extended driven dissipative chain of coupled Duffing oscillators using the classical OTOC to investigate the spread and growth (decay) of an initially localized perturbation in the chain. Correspondingly, we find three distinct types of dynamical behavior: the *sustained chaos, transient chaos*, and *nonchaotic region*, as clearly exhibited by different geometrical shapes in the OTOC heat map. To quantify such differences, we look at *instantaneous speed* (IS), *finite-time Lyapunov exponents* (FTLEs), and *velocity-dependent Lyapunov exponents* (VDLEs) extracted from OTOCs. Introduction of these quantities turns out to be instrumental in diagnosing and demarcating different regimes of dynamical behavior. To gain control over open nonlinear systems, it is important to look at the variation of these quantities with respect to parameters. As we tune drive, dissipation, and coupling, FTLEs and IS exhibit transition between sustained chaos and nonchaotic regimes with intermediate transient chaos regimes and highly intermittent sustained chaos points. In the limit of zero nonlinearity, we present exact analytical results for the driven dissipative harmonic system, and we find that our analytical results can very well describe the nonchaotic regime as well as the late-time behavior in the transient regime of the Duffing chain. We believe that this analysis is an important step forward towards understanding nonlinear dynamics, chaos, and spatiotemporal spread of perturbations in many-particle open systems.

I. INTRODUCTION

Chaotic and regular motion and transition between them with variation of tunable parameters has always been a central issue of interest in the context of dynamical systems. The fact that extreme sensitivity to arbitrarily small perturbations in initial conditions and system parameters may result in complex dynamical behavior has led to extensive studies of chaos in numerous classical [1,2] as well as quantum model systems [3,4]. Needless to say, chaos, being ubiquitous, has found applications in various fields starting from atmospheric sciences [1,5–7], chemical sciences [8–11], biological sciences [12–15], and technological electro-mechanical devices [16–19].

Chaotic behavior in classical systems is diagnosed with the aid of the Lyapunov exponent (LE), λ, which characterizes the rate of separation of initially infinitesimally close trajectories at large times. Depending on the sign of λ, the dynamics is classified as chaotic ($\lambda > 0$) and nonchaotic or regular ($\lambda \leqslant 0$). In addition to this, the phenomenon of chaos is examined using concepts such as phase-space portraits, Poincaré sections, bifurcation diagrams, and power spectrum analysis, to name a few [2,3]. Most of the work along this line has been restricted to systems involving single [20] or very few degrees of freedom at best [21].

In the case of extended systems involving many degrees of freedom, there have been interesting studies concerning not only growth of small localized initial separation but also their spread in space. Examples include propagation of chaos in reaction-diffusion systems [22,23], coupled-map lattices [24,25], the Fermi-Pasta-Ulam (FPU) chain [26,27], high-dimensional coupled symplectic maps [28–30], dilute gases of identical hard balls [31], Brownian motion and microplasmas [32], the complex Ginzburg-Landau system, the Gray-Scott network [33], and coupled phase oscillators [34–36], where both Lyapunov exponents and spatial propagation of perturbation are discussed in the contexts of computing time delayed mutual information and redundancy [22], defining both temporal as well as spatial Lyapunov exponents [24], introducing entropy potential [25], convective Lyapunov spectrum [26], etc.

Recently, a novel promising method, the out-of-time-ordered correlator (OTOC), has been put forward to study spatiotemporal chaos in extended systems [37,38]. This quantity, denoted as $D(x, t)$, measures the growth (in time) and spread (in space) of an infinitesimal localized perturbation in the initial conditions of two copies of the system. Usually the OTOC is presented in the form of a heat map in space-time which has light-cone-like structures [37]. Such structures are described by a ballistic spread and growth of perturbation, characterized by butterfly speed v_b (essentially of the cone) and the Lyapunov exponent λ.

Although this has generated a lot of interest, the use of OTOC as a diagnostic in classical extended systems has been

---

[*]amit.chatterjee@icts.res.in
[†]anupam.kundu@icts.res.in
[‡]manas.kulkarni@icts.res.in

TABLE I. Characterization of the dynamical regimes of a driven dissipative DC. The corresponding figures are mentioned alongside.

	Sustained chaos	Nonchaotic regime	Transient chaos
OTOC $[D(i, \tau)]$	Exponential growth and ballistic spread	Exponential decay and ballistic spread in $D_{\text{th}} \to 0$ limit	Dynamical crossover: exponential growth and ballistic spread $\longrightarrow$ nongrowing and nonspreading OTOC
Heat map structure	*Light cone with sharp boundaries [Fig. 1(a)]*	*Light cone with nonsharp boundaries [Fig. 1(b)]*	*Complex geometric shapes with initial light-cone formation [Figs. 1(c) and 1(d)]*
FTLE $[\lambda_i(\tau)]$	$\lambda_i(\tau \approx 0) < 0$ $\lambda_i(\tau \to \infty) = \lambda > 0$	$\lambda_i(\tau \approx 0) < 0$ $\lambda_i(\tau \to \infty) = \lambda < 0$	$\lambda_i(\tau \approx 0) < 0$ $\lambda_i(\tau)$ crosses from >0 to <0 at finite τ and $\lambda_i(\tau \to \infty) = \lambda < 0$
Number of crossings with $\lambda_i(\tau) = 0$ line (n_c)	$n_c = 1$ (Fig. 3)	$n_c = 0$ (Fig. 8)	$n_c = 2$ (Fig. 11)
IS $[v_b(\tau, D_{\text{th}})]$	Saturates to constant $v_b > 0$, Independent of D_{th} (inset Fig. 7)	Well defined only in $D_{\text{th}} \to 0$ limit (inset Fig. 7)	> 0 for small τ $= 0$ for large τ (inset Fig. 10)
$D_{\text{th}} = 1$	$v_b(\tau \text{ large}, 1) = v_b > 0$ [Fig. 18, $\bar{f} \in (0.25, 1.0)$]	$v_b(\tau \text{ large}, 1) = 0$ [Fig. 18, $\bar{f} \in (0, 0.25)$]	$v_b(\tau \text{ small}, 1) > 0$ & $v_b(\tau \text{ large}, 1) = 0$ (inset Fig. 18)
VDLE $[\lambda(v)]$ $v \lesssim v_b$	$\lambda[1 - (\frac{v}{v_b})^2]$ (Fig. 4)	$\lambda(v) - \lambda \approx 0$ (Fig. 9)	$\lambda[1 - (\frac{v}{v_b})^2]$, small τ (Fig. 13) $\lambda(v) - \lambda \approx 0$, large τ (Fig. 15)
$v \gtrsim v_b$	$\lambda[1 - (\frac{v}{v_b})^{\frac{5}{2}}]$ (Fig. 4)	$(\lambda(v) - \lambda) \sim -(v - v_b)^{\frac{3}{2}}$ (Fig. 9)	$\lambda[1 - (\frac{v}{v_b})^{\frac{5}{2}}]$, small τ (Fig. 13) $(\lambda(v) - \lambda) \sim -(v - v_b)^{\frac{3}{2}}$, large τ (Fig. 15)

restricted to a very few cases, such as classical Heisenberg spin chain at infinite temperature [37], thermalized fluid obeying the Galerkin-truncated inviscid Burgers equation [39], and classical interacting spins on a kagome lattice [40]. It is important to note that *most* of these works were on Hamiltonian systems. Studies in systems lacking a Hamiltonian structure, especially, in driven-dissipative systems, are essentially unexplored. In this paper, we address spatiotemporal chaos in an extended driven dissipative system using a Duffing chain (DC) as a platform.

The idea of an OTOC originates from the fascinating and well-developed notion of an out-of-time-ordered commutator in quantum systems widely used to study scrambling of information and quantum chaos [41–46]. This measures the generation (in space-time) of noncommutativity of otherwise initially commuting operators in extended quantum systems. There have been recent works where out-of-time-ordered commutators play a prominent role. For example, it has been used to understand the effect of dissipation in quantum systems [47,48], to characterize thermal and many-body localized phases [49–51], to understand localization to delocalization transition in quasiperiodic systems (e.g., the Aubry-André model) [52], to study scrambling of information in both integrable and nonintegrable models such as the Sachdev-Ye-Kitaev model [53,54], one-dimensional quantum Ising spin chain [55], Floquet-Frederickson-Anderson model [56], disordered *XY* spin chain [57], and exploring superdiffusive broadening of fronts in long-range power-law interaction systems [58].

Despite this considerable work on extended quantum systems, as mentioned earlier, very little has been investigated

in extended classical Hamiltonians, and essentially nothing is explored in non-Hamiltonian systems. To address this lack of understanding, in this paper, we study spatiotemporal chaos in a *driven dissipative* chain of coupled Duffing chain (DC) oscillators using OTOC. This is a rich nonlinear system which exhibits a plethora of exciting complex dynamical phenomena. In the context of investigating various intriguing phenomena like chaos, multivalued amplitude response, synchronization, and chimera states, to name a few, systems with single or a few Duffing oscillators have been extensively and successfully used as a platform [20,21,59–74]. In addition Duffing oscillators can be used in various practical applications. For example, Duffing oscillator-based encryption devices have been proposed for secure communication systems [75,76]. Duffing oscillators can be used in weak signal detection in various cases like fatigue damage in materials [77,78] and down-hole acoustic telemetry in oilfield exploration [79]. Such broad applications of Duffing oscillators and progress in theory [65] as well as in experiments [76] makes the DC a natural test bed for studying spatiotemporal chaos in extended driven dissipative classical systems, an area yet largely unexplored. Below we briefly summarize our main observations and findings (see also Table I).

(i) We present the OTOC as a remarkable diagnostic for demarcating various regimes of dynamical behaviors of a chain of coupled Duffing oscillators. The space-time heat map plots of it show distinct patterns for the three dynamical regimes, called the *sustained chaos, transient chaos*, and *nonchaotic* regimes (see Fig. 1). Although the existence of these three regimes was known from earlier works [80], a good diagnostic was missing.
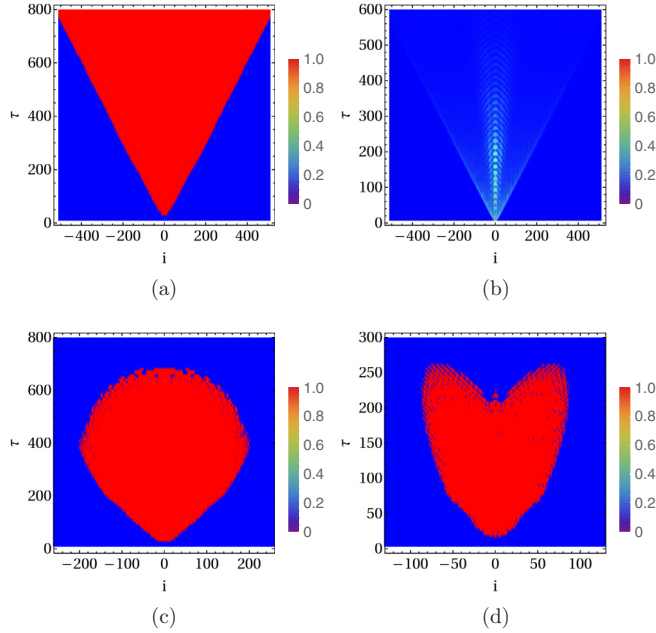
FIG. 1. *OTOC heat maps in different dynamical regimes:* Spatiotemporal spread of perturbation in a driven dissipative Duffing chain (DC) exhibits different dynamical regimes. The OTOC [see Eq. (5)] for a DC of length $N = 1025$ shows (a) ballistic spread and exponential growth forming a *light cone* in the *sustained chaos* regime, (b) short-time ballistic spread and exponential decay creating an initial *light cone* that vanishes rapidly in the *nonchaotic* regime, (c) initial growth and ballistic spread followed by exponential decay and nonballistic behavior, and the initial light cone deforms into a *balloon* shape in the *transient chaos* regime, and (d) similar qualitative behavior as in (c), only the initial light-cone deforms into a *butterfly* shape in the *transient chaos* regime. Initially ($\tau = 0$) the middle oscillator ($i = 0$) is perturbed with $\epsilon = 10^{-6}$. Parameters used for panels (a), (b), (c), and (d) are, respectively, $\{\bar{f} = 0.30, \bar{\gamma} = 0.15, \bar{\kappa} = 1.0\}$, $\{\bar{f} = 0.09, \bar{\gamma} = 0.01, \bar{\kappa} = 2.0\}$, $\{\bar{f} = 0.24, \bar{\gamma} = 0.15, \bar{\kappa} = 1.0\}$, and $\{\bar{f} = 0.13, \bar{\gamma} = 0.15, \bar{\kappa} = 1.0\}$.

(ii) Given that the heat map plots can be different from the conventional light-cone-type maps (see Fig. 1), it necessitates generalizing the notion of concepts such as the butterfly velocities and the Lyapunov exponents. More precisely, we introduce the notion of *instantaneous butterfly speed* (IS) and use the generalized notion of the finite-time Lyapunov exponent (FTLE) [27]. These notions proved to be key for understanding finite-time behavior and transitions between different dynamical regimes.

(iii) We observe that in the sustained chaos regime, the growth of the perturbation measured in a frame moving with speed v is exponential with a Lyapunov exponent $\lambda(v)$ dependent on v. Such a velocity-dependent Lyapunov exponent, known as a VDLE [38] or convective LE [26], has been studied recently [37,38], where it was observed that $\lambda(v)$ depends linearly on v for $v \sim v_b$. In our case also, we observe such linear dependence. However, interestingly, the *detailed form* of the VDLE for a DC has been observed to be different from what has been reported earlier for chaotic Hamiltonian systems [37,38,40].

(iv) In the transient chaos regime, the OTOC grows initially (as a conventional light cone), which is characterized by FTLEs. After this initial dynamics, there is a simultaneous decrease in the FTLE at a specific time in all oscillators that have gained a positive FTLE by this time. This effect is manifested in the corresponding OTOC heat map as emergence of complex geometrical shapes. We also find that once there is this decrease, the subsequent features can be quantitatively explained via analytical results from a driven dissipative harmonic chain (HC).

(v) The variation of the IS and FTLE with tunable parameters exhibits several interesting features. With the continuous increase of the driving amplitude, the DC transits from a nonchaotic to sustained chaos regime. This transition, interestingly, is preceded by the appearance of intermittent transient chaos windows and sustained chaos points inside the nonchaotic regime. Deep inside the sustained chaos regime, the FTLE (that, in the large time limit, saturates to the conventional Lyapunov exponent) increases linearly with driving amplitude. In the case of tuning the dissipation, stating from a chaotic regime, the FTLE decreases approximately linearly with increasing dissipation followed by a highly intermittent behavior with a mixture of chaotic and periodic windows. In the context of coupling, our investigation reveals that a chain of uncoupled Duffing oscillators in the nonchaotic regime can be made to transit to the chaotic regime only by tuning the coupling strength. Also, the IS exhibits a power-law increase ($v_b \sim \kappa^\sigma$ with $\sigma = 0.71$) with increasing coupling strength. Notably, the value of σ for the DC is different from that of $\sigma = 1/2$ in the case of a driven dissipative HC (shown analytically in Appendix A). This indicates the important role of nonlinearity in the speed of spatial spread of an initially localized perturbation.

(vi) For the case of zero nonlinearity, i.e., for a driven dissipative HC, we present rigorous analytical results for the OTOC and VDLE (Appendix A). Results for the OTOC are obtained in terms of the Airy function, and the effect of openness (dissipation) is elaborated. The behavior of VDLEs is extracted.

II. MODEL AND TOOLS (OTOC, IS, FTLE)

We consider a driven dissipative ring of N Duffing oscillators, with nearest-neighbor harmonic coupling where every oscillator is coherently driven by an external periodic force of frequency Ω and strength f. The equation of motion for the ith oscillator with position $x_i(t)$ at time t is given by

$$\ddot{x}_i = k_0 x_i - \alpha x_i^3 - \gamma \dot{x}_i + \kappa(x_{i+i} + x_{i-1} - 2x_i) + f\cos(\Omega t), \tag{1}$$

where $\alpha, \gamma, \kappa, k_0$ are nonlinearity, damping, harmonic coupling constant, and spring constant, respectively. We need $\alpha > 0$ to ensure that the on-site potential is confining. Also note that $\gamma > 0$ to make sure that the system does not heat up. We restrict ourselves to $k_0 > 0$ to make the on-site potential double-well in nature. For this model, we aim to study the possibility of chaotic, transient, and regular motions of this spatially extended chain of Duffing oscillators in the parameter space constituted by $\{f, \gamma, \kappa, \alpha, \Omega, k_0\}$ using the OTOC as a tool.

To start, it is important to note that using proper scaling it is possible to reduce the number of independent scaling parameters. We define the new variables

$$y_i = \sqrt{\alpha}\, x_i, \ \tau = \sqrt{k_0}\, t, \qquad (2)$$

so that Eq. (1) gets transformed into

$$\ddot{y}_i = y_i - y_i^3 - \bar{\gamma}\dot{y}_i + \bar{\kappa}(y_{i+1} + y_{i-1} - 2y_i) + \bar{f}\cos(\bar{\Omega}\tau), \ (3)$$

where

$$\bar{\gamma} = \frac{\gamma}{\sqrt{k_0}}, \ \bar{\kappa} = \frac{\kappa}{k_0}, \ \bar{f} = \frac{f}{k_0}\sqrt{\alpha}, \ \bar{\Omega} = \frac{\Omega}{\sqrt{k_0}}. \qquad (4)$$

In order to explore different dynamical behaviors of the extended DC we study the OTOC in this rich parameter space.

To measure the OTOC, we start with two identical copies (I and II) of the same DC with the only difference being an infinitesimal difference ϵ in the initial conditions at a chosen oscillator (say, the middle one). We now let the two copies evolve independently according to Eq. (3) and observe the initial difference spread and growth in space-time, which can be captured by the OTOC [$D(i, \tau)$] defined as

$$D(i, \tau) = \frac{\left|y_i^I(\tau) - y_i^{II}(\tau)\right|}{\left|y_{\text{middle}}^I(0) - y_{\text{middle}}^{II}(0)\right|} = \frac{\left|y_i^I(\tau) - y_i^{II}(\tau)\right|}{|\epsilon|}, \quad (5)$$

This quantity measures the ratio of the deviation between the two copies for the ith oscillators at time τ to the deviation ϵ for the middle oscillator at $\tau = 0$. The OTOC can also be measured for momentum degrees of freedom.

To diagnose chaos in quantum mechanical systems, a widely used tool is the out-of-time-ordered commutator [41–46], which is mathematically defined as $\langle[\hat{A}_x(\tau), \hat{B}_0(0)]^2\rangle$ where $\langle \cdots \rangle$ is taken in a given quantum state. This quantity measures the effect of an operator $\hat{B}_0(0)$ on another operator $\hat{A}_x(\tau)$ at some later time τ where the operators are localized initially around 0 and x, respectively. Since the commutator $[\hat{A}_x(\tau), \hat{B}_0(0)]^2$ contains terms like $\hat{A}_x(\tau)\hat{B}_0(0)\hat{A}_x(\tau)\hat{B}_0(0)$ which are not time ordered, it is called an out-of-time-ordered commutator. For studying chaos in classical systems with a similar approach, a natural quantity would be the corresponding Poisson bracket, i.e., replacing $\frac{1}{i\hbar}[\hat{A}_x(\tau), \hat{B}_0(0)]$ by $\{A_x(\tau), B_0(0)\}$. Considering the observables A and B to be the position $y_i(\tau)$ of the ith oscillator and momenta $p_j(0)$ of the initially perturbed jth (middle) oscillator, respectively, this Poisson bracket provides $\{y_i(\tau), p_j(0)\} = \frac{\partial y_i(\tau)}{\partial y_j(0)} \approx \frac{\delta y_i(\tau)}{\delta y_j(0)}$. Our OTOC defined in Eq. (5) is then expressed in terms of the Poisson bracket as $D(i, \tau) = \sqrt{(\{y_i(\tau), p_j(0)\})^2} = |\frac{\partial y_i(\tau)}{\partial y_j(0)}| \approx |\frac{y_i^I(\tau) - y_i^{II}(\tau)}{y_j^I(0) - y_j^{II}(0)}|$.

Naturally, $D(i, \tau)$ captures information of both the temporal growth (or decay) and spatial spread of the initial deviation. To extract this information, we define IS $v_b(\tau, D_{\text{th}})$ and FTLE $\lambda_i(\tau)$ from the OTOC $D(i, t)$ as

$$v_b(\tau, D_{\text{th}}) = \frac{\sum_{i=1}^{N} \Theta[D(i, \tau) - D_{\text{th}}]}{\tau}, \qquad (6)$$

$$\lambda_i(\tau) = \frac{\ln D(i, \tau)}{\tau}, \qquad (7)$$

where $\Theta(x)$ is a step function. The IS $v_b(\tau, D_{\text{th}})$ in the above equation measures the number of oscillators (per unit time) that have gained deviations greater than or equal to ϵD_{th}. On

the other hand, FTLE $\lambda_i(\tau)$ describes how the deviation at a particular oscillator grows or decays with time. However, it should be emphasized that the FTLEs defined in Eq. (7) are somewhat different from the Lyapunov exponents defined and computed conventionally [81]. In the conventional approach, the exponents are determined from the eigenvalues of the Jacobian matrix obtained from the linearized approximations of the dynamical equations of the system, which characterize the exponential growths (or decays) of infinitesimal deviations in the initial condition [81] along the directions of the eigenvectors, whereas in our case, the FTLE measures the growth (or decay) of the initial perturbation in the original dynamical variables $\delta y_i(\tau) = |y_i^I(\tau) - y_i^{II}(\tau)|$ themselves. Since the variables δy_i can be written as a linear combination of the eigenvectors of the Jacobian, it is evident that the conventional Lyapunov exponents and the FTLEs are related. In fact, at large times all the FTLEs would converge to the maximum Lyapunov exponent computed in the conventional way.

As mentioned earlier, the extended DC exhibits three different types of dynamical behavior: sustained chaos, transient chaos, and nonchaotic behavior. It is exciting to see how IS and the FTLE can characterize and distinguish between all these dynamical regimes. In the case of sustained chaos, one would expect that, in the long τ limit, $\lambda_i(\tau)$ will eventually saturate to some positive constant λ independent of i. Based on recent works on Hamiltonian systems [37,40], the IS is also expected to approach a constant value (time independent), v_b, which is known as the butterfly speed. On the other hand, in the nonchaotic (regular) regimes it is expected that $\lambda_i(\tau) \leqslant 0 \ \forall \tau, i$ and saturates to $\lambda \leqslant 0$ for large τ. However, the notion of butterfly speed for the nonchaotic regime, strictly speaking, ceases to exist. Nonetheless, one can define a spreading speed in the $D_{\text{th}} \to 0$ limit. The transient regime exhibits intricate interplay between nonlinearity, dissipation, and drive. This regime shows a crossover from chaotic dynamics to regular dynamics. This crossover is characterized by a change in sign of the FTLE from positive to negative.

To explore these features, in the next section, we numerically compute IS and the FTLE from the OTOC and analyze in detail how they can describe the three different dynamical regimes in the DC.

III. NUMERICAL RESULTS

In this section we numerically compute the OTOC defined in Eq. (5) in the $\epsilon \to 0$ limit. In this limit, one can in fact write an evolution equation for $\delta y_i(\tau) = y_i^I(\tau) - y_i^{II}(\tau)$, which to leading order in ϵ is given by

$$\frac{d^2\delta y_i}{d\tau^2} = \left(1 - 3y_i^2\right)\delta y_i - \bar{\gamma}\frac{d\delta y_i}{d\tau} + \bar{\kappa}(\delta y_{i+i} + \delta y_{i-1} - 2\delta y_i), \tag{8}$$

where $y_i(\tau)$ present in the first term is obtained by solving Eq. (3). This term makes this equation a linear ODE with time-dependent coefficient, and this is the central cause of possible spread and growth of the OTOC. To integrate Eqs. (3) and (8) numerically, we use the fourth-order Runge-Kutta (RK4) algorithm with time step $\Delta\tau = 0.001$ and with initial
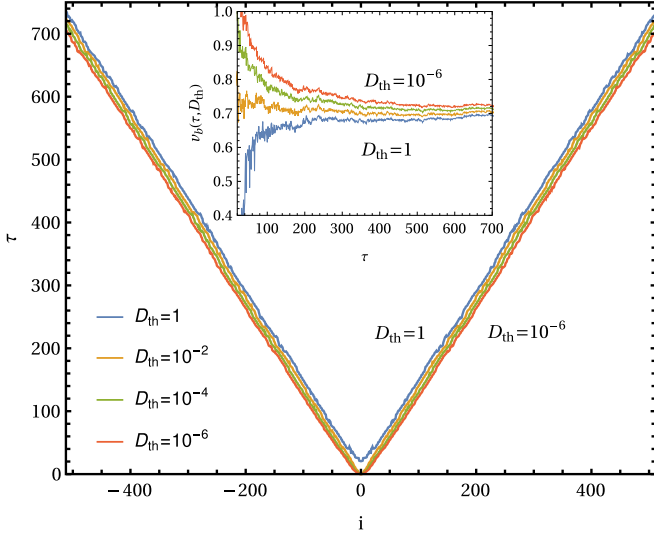
FIG. 2. *Light-cone boundaries and IS for different D_{th} in the sustained chaos regime:* The main plot shows the boundaries of the OTOC light cone for different values of threshold (D_{th}) lie very close, implying the ballistic spread is independent of D_{th}. In the inset plot, the slopes [$v_b(\tau, D_{th})$] of these boundaries computed from Eq. (6) are indeed observed to be independent of the value of D_{th}, and they saturate to a constant butterfly speed $v_b = 0.7$. Parameters used are $\{\bar{f} = 0.30, \bar{\gamma} = 0.15, \bar{\kappa} = 1.0\}$.

conditions

$$y_i(0) = y_0, \quad \dot{y}_i(0) = 0,$$
$$\delta y_i(0) = \epsilon \, \delta_{i,0}, \quad \delta \dot{y}_i(0) = 0,$$

(9)

for $i = -\lfloor(N-1)/2\rfloor, \ldots, ts - 1, 0, 1, \ldots, \lfloor(N-1)/2\rfloor$ where y_0 is a constant and $\delta_{i,j}$ is the usual Kronecker δ function. Here $\lfloor..\rfloor$ is the floor function. Note that the deviation $\delta y_i(0)$ is nonzero only at the middle site, which can be thought of as an initial perturbation. For all numerical simulations, we chose $\epsilon = 10^{-6}$ and $\bar{\Omega} = 1$. The space constituted by the other three parameters $\{\bar{f}, \bar{\gamma}, \bar{\kappa}\}$ are explored extensively to investigate the three different dynamical regimes.

A. Sustained chaos regime

In this case, we carefully choose the parameter values to be $\{\bar{f} = 0.30, \bar{\gamma} = 0.15, \bar{\kappa} = 1.0\}$ with $y_0 = 0.3$ to observe the sustained chaos regime in a DC of length $N = 1025$. In Fig. 1(a) we present the heat map of $D(i, \tau)$, which exhibits a *light-cone*-like structure implying ballistic propagation of perturbation along the chain. The speed of the propagation can, in principle, be obtained from the slope of the boundary between the dark and bright regions of the heat map. Instead of using this method, we employ a more accurate method of determining the boundary line. At a given τ we find the farthest oscillator i from the middle in either direction such that $D(j, \tau) < D_{th}$ for $|j - (N+1)/2| > |i - (N+1)/2|$. We plot such boundaries for different D_{th} in Fig. 2, and we observe that the slopes of these boundary lines are independent of D_{th}. An equivalent way of extracting this speed is by computing the IS defined in Eq. (6), and this is plotted in the inset of Fig. 2, where we see that it saturates to $v_b = 0.7$.
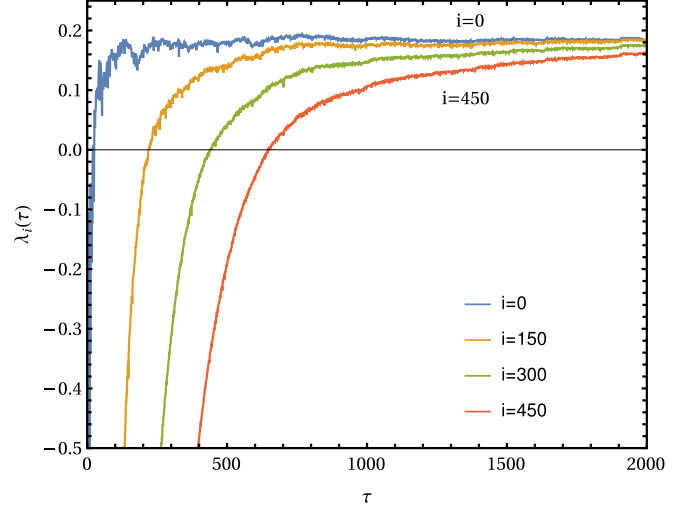

FIG. 3. *FTLE vs time in the sustained chaos regime:* the FTLE [computed from Eq. (7)] for different oscillators (i) saturates to the same constant value, the conventional Lyapunov exponent $\lambda_i(\tau) = \lambda = 0.18$ identifying the exponential growth of the OTOC. Parameters used are $\{\bar{f} = 0.30, \bar{\gamma} = 0.15, \bar{\kappa} = 1.0\}$.

To measure the rate of growth of the perturbation, in Fig. 3 we plot FTLE $\lambda_i(\tau)$ for different values of i. We observe that in the large τ limit the FTLEs for all the oscillators reach the conventional Lyapunov exponent λ, which, for the parameter set $\{\bar{f} = 0.30, \bar{\gamma} = 0.15, \bar{\kappa} = 1.0\}$, has the value $\lambda = 0.18$. This implies that the initial perturbation localized at the middle point grows exponentially with time and spreads to all the oscillators, making the whole DC chaotic. The fact that the FTLEs for all the oscillators reach $\lambda > 0$ and stay there ensures that the DC sustains its chaotic behavior indefinitely.

The facts that the OTOC grows exponentially and spreads ballistically suggest that the OTOC has the following scaling form:

$$\lim_{\tau \to \infty} \frac{\ln D(i, \tau)}{\tau} = \lim_{\tau \to \infty} \lambda_i(\tau) = \lambda(i/\tau) = \lambda(v),$$

(10)

which we verify numerically in Fig. 4 via excellent data collapse. Existence of such a scaling function implies that the perturbation observed in a frame moving with a velocity $v = i/\tau$ also grows or decays exponentially with a velocity-dependent Lyapunov exponent (VDLE) $\lambda(v)$. Concepts similar to the VDLE have been introduced earlier in the context of finite group velocity (Lieb-Robinson bound) in quantum spin systems with finite range interactions [82]. These velocity-dependent exponents, also known as the convective Lyapunov spectrum [26], have been reported in studies of coupled map lattices [83,84], complex Ginzburg-Landau equation [85], FPU chain [26], classical Heisenberg spin chain [37], interacting spins on kagome lattice [40], etc.

Interestingly, a universal framework for describing exponential growth or decay of OTOCs in classical, semiclassical, and large-N systems in terms of the VDLE has recently been discussed in Ref. [38], and possible functional forms of $\lambda(v)$ for $v \sim v_b$ have been proposed. In particular, for chaotic classical systems, it has been analyzed that $\lambda(v)$ continuously approaches zero both from inside and outside the
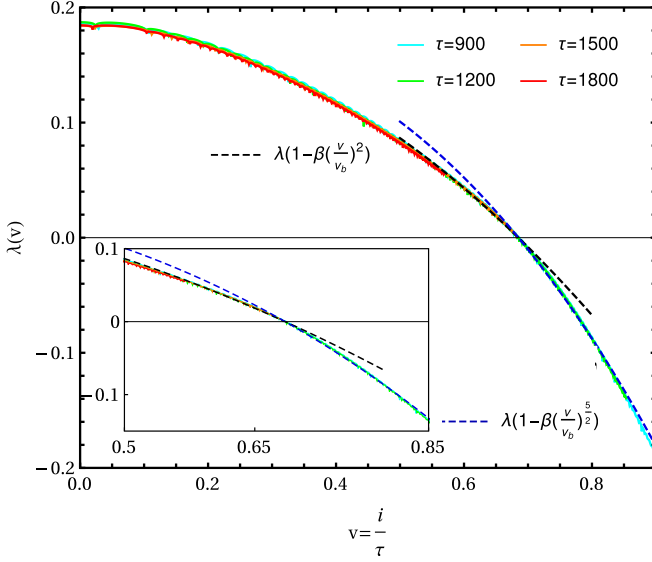
FIG. 4. *VDLE near $v \approx v_b$ in sustained chaos regime:* the VDLE [see Eq. (10)] exhibits a linear dependence $\lambda(v) \sim (v - v_b)$ near $v \approx v_b$. However, for $v \lesssim v_b$ and $v \gtrsim v_b$, $\lambda(v)$ falls off with different exponents, $\lambda(v) = \lambda[1 - (\frac{v}{v_b})^\nu]$ with $\nu = 2$ and $\nu = \frac{5}{2}$, respectively. To show the existence of these two different exponents more prominently, in the inset we present a magnified version of the main plot in $0.5 \leqslant v \leqslant 0.85$. Here $v_b = 0.69$ and $\lambda = 0.18$. Parameters used are $\{\bar{f} = 0.30, \bar{\gamma} = 0.15, \bar{\kappa} = 1.0\}$.

light cones as $\lambda(v) \sim |v - v_b|$. Such linear behavior has been verified for Hamiltonian systems [37], e.g., in a classical Heisenberg chain [37] where it has been observed that $\lambda(v) = \lambda[1 - (v/v_b)^2]$. All these results and discussions are mostly restricted to Hamiltonian systems. Therefore one ponders as to how the VDLE $\lambda(v)$ would behave for driven dissipative systems.

Motivated by the observations $\lambda(v) = \lambda[1 - (v/v_b)^2]$ for $v \approx v_b$ in classical spin chains [37,40], one could ask if the same relation also holds for other models. In particular, the situation for a driven dissipative system is even more elusive. Nonetheless, we use this form of $\lambda(v)$ for the DC and obtain the following exponents (see Fig. 4):

$$\lambda(v) = \begin{cases} \lambda[1 - (v/v_b)^2], & \text{for } v \lesssim v_b \\ \lambda[1 - (v/v_b)^{5/2}], & \text{for } v \gtrsim v_b \end{cases}. \quad (11)$$

So, as seen in the context of Hamiltonian systems [37,38], the function $\lambda(v)$ in our case goes to zero linearly as v approaches v_b. This is evident from the Taylor series expansion, i.e., $\lambda[1 - (\frac{v}{v_b})^\nu] \approx \lambda \nu (1 - \frac{v}{v_b})$ where $\nu = 2$ for $v < v_b$ and $\nu = 5/2$ for $v > v_b$. These differences in the slopes are prominent from both Figs. 5(a) and 5(b) (for $\tau = 900$ and $\tau = 1200$, respectively), where we have plotted $|\log(1 - \frac{\lambda(v)}{\lambda})|$ as a function of $|\log(\frac{v}{v_b})|$ near $v = v_b$. The slopes for these plots yield $\nu \approx 2.5$ for $v > v_b$ whereas $\nu \approx 2$ for $v < v_b$. It is natural to ask if the VDLE for the DC has some single functional form that holds for both $v < v_b$ and $v > v_b$. In this regard we find

$$\lambda(v) = \lambda[1 - \beta(v/v_b)^2 - \delta(v/v_b)^4 - (1 - \beta - \delta)(v/v_b)^6],$$
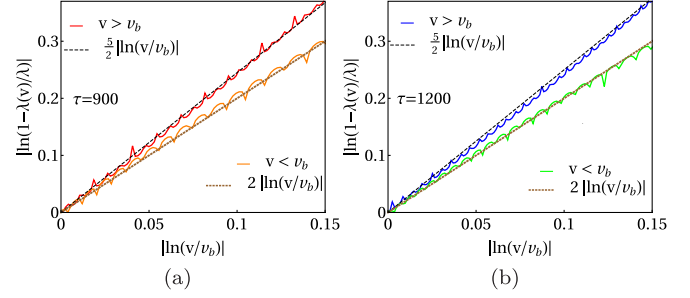$$\beta = 1.2, \quad \delta = -0.5, \quad (12)$$

FIG. 5. *Different VDLE exponents for $v < v_b$ and $v > v_b$ seen clearly in a log-log scale:* The slopes are 2 and 5/2 for $v < v_b$ and $v > v_b$, respectively, as seen in the fitting in Fig. 4. Parameters used are $\{\bar{f} = 0.30, \bar{\gamma} = 0.15, \bar{\kappa} = 1.0\}$.

which is clearly depicted in Fig. 6. Note that the coefficient in the last term of Eq. (12) is fixed because of the constraint $\lambda(v = v_b) = 0$. One might ask if the different exponent values observed in case of the DC in comparison to the Hamiltonian system in Ref. [37] is arising due to the presence of drive and dissipation. To answer this, in the inset of Fig. 6, we present the behavior of $\lambda(v)$ for $\bar{f} = 0$ and $\bar{\gamma} = 0$. We observe that it still deviates from the behavior of VDLE in the case of the Heisenberg spin chain in Ref. [37] and has the functional form $\lambda(v) = \lambda[1 - \beta(v/v_b)^2 - (1 - \beta)(v/v_b)^4]$ with $\beta = 0.613$.

The facts that (i) the VDLE can behave differently for different Hamiltonian systems and (ii) the introduction of drive and dissipation has further significant impact on the behavior
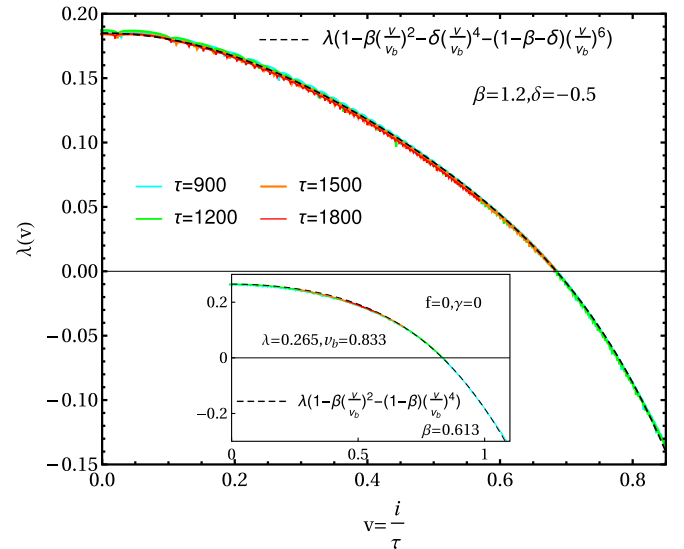

FIG. 6. *VDLE vs v in sustained chaos regime fitted for a wider region of v:* For any value of v (not necessarily in the neighborhood of v_b), the VDLE for the DC follows the functional form $\lambda(v) = \lambda[1 - \beta(v/v_b)^2 - \delta(v/v_b)^4 - (1 - \beta - \delta)(v/v_b)^6]$ with $\beta = 1.2$ and $\delta = -0.5$. In the inset, the corresponding Hamiltonian counterpart with $\bar{f} = 0$ and $\bar{\gamma} = 0$ is plotted, and we observe that the VDLE in this case has a different expression given by $\lambda(v) = \lambda[1 - \beta(v/v_b)^2 - (1 - \beta)(v/v_b)^4]$ with $\beta = 0.613$. Parameters used are $\{\bar{f} = 0.30, \bar{\gamma} = 0.15, \bar{\kappa} = 1.0\}$.
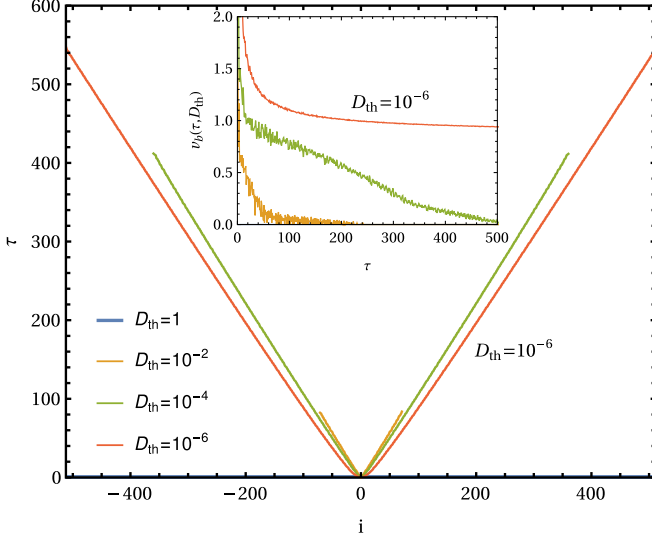
FIG. 7. *Light-cone boundaries and IS for different D_{th} in nonchaotic regime:* The main plot shows the boundaries of the OTOC here strongly depend on D_{th}, and the smaller the D_{th} value, the larger is the light-cone boundary. In the inset, we observe that the slopes (IS) of the corresponding boundaries, computed from Eq. (6), have well-defined values only in the $D_{th} \to 0$ limit. In particular $v_b(\tau) = 0.93$ for $D_{th} = 10^{-6}$, whereas $v_b(\tau) \approx 0$ for $D_{th} = 1$. Parameters used are $\{\bar{f} = 0.09, \bar{\gamma} = 0.01, \bar{\kappa} = 2.0\}$.

of $\lambda(v)$ are interesting observations and require further exploration.

B. Nonchaotic regime

The DC possess a nonchaotic regime characterized by a nongrowing OTOC. In Fig. 1(b) we give the OTOC heat map for $\{\bar{f} = 0.09, \bar{\gamma} = 0.01, \bar{\kappa} = 2\}$ in a DC of length $N = 1025$. In this map we find there is a light-cone-like structure, but importantly the boundary separating the regions inside and outside the cone ceases to exist at larger times. Therefore in this regime, strictly speaking the propagation speed defined in Eq. (6) is defined only in the $D_{th} \to 0$ limit. This is seen in Fig. 7, where we plot the boundary measured with different values of D_{th}, and we find that smaller the threshold, the larger the length of the boundary (implying that further oscillators feel a smaller amount of perturbation). Hence the slope of the boundary gets a well-defined value for propagation speed as $D_{th} \to 0$. The same value is also obtained from direct computation of the propagation speed from Eq. (6) for a very small D_{th} as presented in the inset plot of Fig. 7. Note that the velocity obtained from the slope and from Eq. (6) may be different for finite D_{th}, but they match in the limit $D_{th} \to 0$.

In Fig. 8 we plot $\lambda_i(\tau)$ versus τ for different oscillators, and we observe that they all saturate to a negative value, because dissipation dominates in this regime. Mathematically, $\lambda_i(\tau \to \infty) = \lambda < 0 \ \forall i$.

Motivated by our findings regarding the VDLE in the sustained chaos case, we, in this case, explore how $\lambda(v)$ scales with respect to τ and behaves as function of $v = i/\tau$. To investigate this, we present the corresponding numerical results in Fig. 9, where we plot $\lambda(v)$ [as defined in Eq. (10)] as a
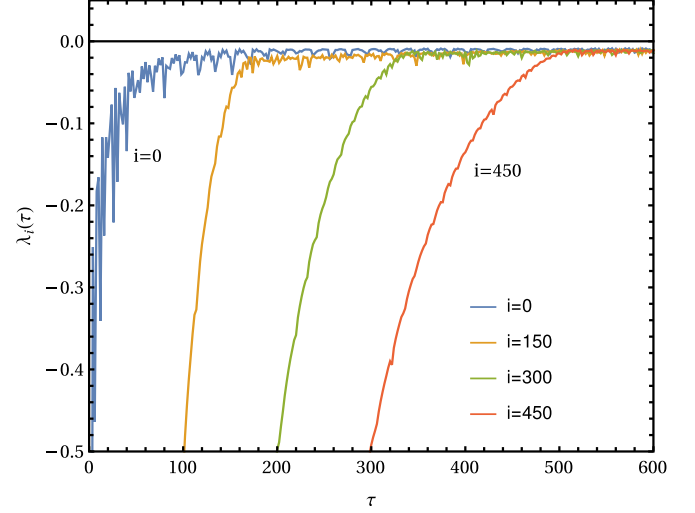

FIG. 8. *FTLE vs time in nonchaotic regime:* the FTLE [computed from Eq. (7)] for different oscillators (i) saturates to the same negative constant, the conventional Lyapunov exponent $\lambda_i(\tau) = \lambda = -0.01$ identifying the exponential decay of the OTOC. Parameters used are $\{\bar{f} = 0.09, \bar{\gamma} = 0.01, \bar{\kappa} = 2.0\}$.

function of v. There, along with excellent data collapse at a different time, we observe that

$$\lambda(v) = \begin{cases} \lambda, & \text{for } v < v_b \\ \lambda - (v - v_b)^{\frac{3}{2}}, & \text{for } v > v_b \end{cases}, \quad (13)$$

where $\lambda_0 = \lambda$.

At this point it is worth noting that same behavior for the VDLE has been recently reported in Ref. [38] for nonchaotic noninteracting Hamiltonian systems. In the nonchaotic regime, the dynamics in our problem becomes essentially a linear HC (noninteracting) because the particles
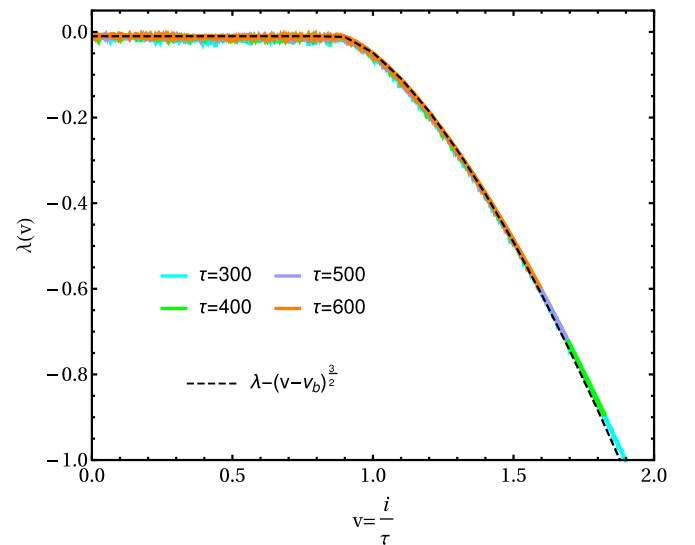

FIG. 9. *VDLE in nonchaotic regime and comparison to analytical results from harmonic approximation:* $\lambda(v)$ is always negative in the nonchaotic case. It is almost constant ($\lambda(v) = -0.01$) inside the cone ($v \leqslant v_b = 0.886$) and falls as $(\lambda(v) - \lambda) \sim -(v - v_b)^{3/2}$ outside the cone ($v \geqslant v_b$). Parameters used are $\{\bar{f} = 0.09, \bar{\gamma} = 0.01, \bar{\kappa} = 2.0\}$.

execute small oscillations around the minima of the double-well potential, i.e., $y_i^2 \approx 1$. As a result the equation for the perturbation δy_i in Eq. (8) becomes

$$\frac{d^2 \delta y_i}{d\tau^2} = -k_0 \delta y_i - \bar{\gamma} \frac{d\delta y_i}{d\tau} + \bar{\kappa}(\delta y_{i-1} + \delta y_{i+1} - 2\delta y_i), \quad (14)$$

with $k_0 = 2$, where we have neglected the cubic term due to its smallness. In what follows, we demonstrate analytically that above equations of motion of a chain of coupled HC oscillators exhibit the behavior in Eq. (13) even in presence of dissipation for arbitrary $k_0 > 0$. It is also to be noted that although the original particle dynamics in Eq. (3) is subjected to both drive and dissipation, the dynamics of the perturbation becomes insensitive to the drive because $y_i^2 \approx 1$ at all times.

Writing the general solutions for δy_i in Eq. (14) exactly and using them in Eq. (5), we obtain the following expression for the OTOC in a HC (see Appendix A for details):

$$D(i, \tau) = \frac{e^{-\bar{\gamma}\tau/2}}{N} \sum_{j=1}^{N} \left[\cos\left(\frac{2\pi i j}{N} - \Delta_j \tau \right) \right.$$
$$\left. + \frac{\bar{\gamma}}{2\Delta_j} \sin\left(\frac{2\pi i j}{N} - \Delta_j \tau \right) \right], \quad (15)$$

where $\Delta_j = \sqrt{4\bar{\kappa} \sin^2(\frac{\pi j}{N}) + k_0 - (\frac{\bar{\gamma}}{2})^2}$. For a spatially extended large system, in the limit $N \to \infty$, one can take the continuum limit of Eq. (15) by letting $\frac{\pi j}{N} = q$ so that

$$D(i = v\tau, \tau) = \frac{e^{-\frac{\bar{\gamma}\tau}{2}}}{\pi} \times \int_0^{\pi} dq \left\{ \cos\left[2\tau\left(qv - \frac{1}{2}\Delta_q \right) \right] \right.$$
$$\left. - \frac{\bar{\gamma}}{2\Delta_q} \sin\left[2\tau\left(qv - \frac{1}{2}\Delta_q \right) \right] \right\},$$

where $\Delta_q = \sqrt{2\bar{\kappa}} \sqrt{1 + \eta - \cos(2q)}$ with $\eta = \frac{k_0 - (\bar{\gamma}/2)^2}{2\bar{\kappa}}$. A saddle point approximation of the integrand yields (see again Appendix A for details)

$$D(v\tau, \tau) = \begin{cases} \frac{2e^{-\frac{\bar{\gamma}\tau}{2}} g(q^*)}{(4v_b\tau)^{1/3}} \mathrm{Ai}(z), & \text{for } v \gtrsim v_b \\ \frac{2e^{-\frac{\bar{\gamma}\tau}{2}} g(q^*)}{(4v_b\tau)^{1/3}} \mathrm{Ai}(-z), & \text{for } v \lesssim v_b \end{cases}$$

$$\text{with } z = \frac{2^{\frac{1}{3}} |v_b - v| \tau^{\frac{2}{3}}}{v_b^{\frac{1}{3}}} > 0, \quad (16)$$

where $\mathrm{Ai}(z)$ is the Airy function. Here $v_b = \sqrt{\bar{\kappa}} \sqrt{1 + \eta - \sqrt{(1+\eta)^2 - 1}}$ and $g(q^*, \tau) = \cos[2\tau(vq^* - \frac{1}{2}\Delta_{q^*})] - \frac{\bar{\gamma}}{2\Delta_{q^*}} \sin[2\tau(vq^* - \frac{1}{2}\Delta_{q^*})]$ with q^* given by the solution of $\cos(2q^*) = (1+\eta) - \sqrt{(1+\eta)^2 - 1}$.

In the limit $\tau \to \infty$, using the large z asymptotic of Airy functions, we have

$$D(v\tau, \tau) = \begin{cases} \frac{\hat{g}(q^*, \tau)}{2\sqrt{\tau}} e^{-\frac{\bar{\gamma}}{2}\tau - \frac{2^{\frac{5}{2}}}{3\sqrt{v_b}} \tau(v-v_b)^{\frac{3}{2}}}, & v > v_b \\ \frac{e^{-\frac{\bar{\gamma}\tau}{2}} \hat{g}(q^*, \tau)}{\sqrt{\tau}} \sin\left[\frac{\pi}{4} + \frac{2^{\frac{5}{2}}\tau}{3\sqrt{v_b}}(v-v_b)^{\frac{3}{2}} \right], & v < v_b \end{cases}, \quad (17)$$

where $\hat{g}(q^*, \tau) = \frac{g(q^*, \tau)}{2^{-\frac{3}{4}} \sqrt{\pi}(v-v_b)^{\frac{1}{4}} v_b^{\frac{1}{4}}}$. Notably in Eq. (17), apart from the explicit exponential dependence of the OTOC on dissipation (as $e^{-\bar{\gamma}\tau/2}$), $D(v\tau, \tau)$ depends on γ through $v_b(\bar{\gamma})$ and $q^*(\bar{\gamma})$ in a nontrivial way. We find that the greater the dissipation (γ), the greater is the butterfly velocity. This might seem counterintuitive at first. Note that this measures how far a perturbation (however small it may be) can reach rather than the magnitude of the perturbation. In fact, the magnitude of the perturbation reached is suppressed exponentially with time. From Eq. (17), it is easy to see that the VDLE $\lambda(v)$ defined in Eq. (10) is given by Eq. (13).

It is quite intriguing that, although the DC is a non-Hamiltonian nonlinear system, the VDLE for the DC, in the nonchaotic regime, exhibits same exponents as reported for noninteracting integrable Hamiltonian systems [38].

C. Transient chaos regime

In Secs. III A and III B we have observed that the DC can exhibit sustained chaos or nonchaotic behavior depending on the choices of parameter values $\{\bar{f}, \bar{\gamma}, \bar{\kappa}\}$. The sustained chaos scenario is described by the OTOC growing exponentially and spreading ballistically. On the other hand, the nonchaotic regime is characterized by the OTOC always decaying exponentially and spreading ballistically at short time. In the sustained chaos regime, the FTLE starting from a negative value grows and finally saturates to a positive constant value, whereas in the nonchaotic regime the FTLE always remains negative.

In this section we demonstrate that by choosing the parameters carefully, one can observe a dynamical crossover from an exponentially growing and spreading OTOC (similar to sustained chaos) regime to a nongrowing and nonspreading OTOC (similar to nonchaotic) regime as time progresses. This interesting temporal crossover stems from the crucial presence of both drive and dissipation and is manifested by unconventional heat maps of the OTOC as shown in Figs. 1(c) and 1(d). The existence of such a transient regime is far from obvious and has not been reported in generic Hamiltonian systems. In the context of the DC (non-Hamiltonian), hints about the existence of such regimes have been reported in Ref. [80] based on the observations of trajectories of the oscillators. Using diagnostics based on the OTOC and FTLE, our study reveals that this transient regime can be well characterized and contains in it a zoo of features as described below.

By optimum choice of parameters one can ensure being in the transient chaos regime. As a sample example, we choose $\{\bar{f} = 0.24, \bar{\gamma} = 0.15, \bar{\kappa} = 1.0\}$ with $y_0 = 0.3$ in the DC of length $N = 1025$. The heat map corresponding to these parameters in Fig. 1(c) shows that there is an initial time window $(0 \leqslant \tau < \tau^*)$ in which the DC shares similarities with that of a chaotic system, characterized by light-cone-like structure with sharp boundaries with a certain slope. There is a sudden behavioral change at $\tau = \tau^*$ after which the slope starts being time dependent, thereby creating a sharp corner at $\tau = \tau^*$. This heat map continues to spread, however, with a time-dependent speed till some time $\tilde{\tau}$ after which it stops spreading further. This rich behavior naturally demands a
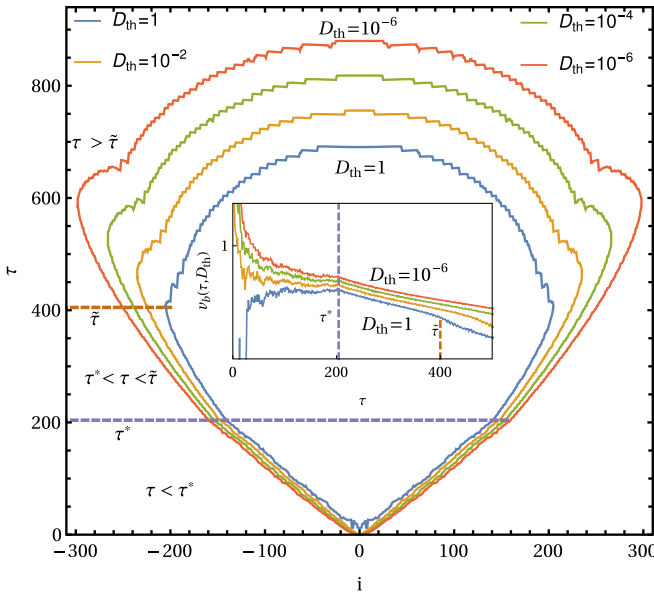
FIG. 10. *Light-cone boundaries and IS for different D_{th} in transient chaos regime:* The main plot shows the boundaries of the OTOC for different values of D_{th}. Initially up to $\tau \approx 204$, the ballistic spread forms light cones, and the boundaries are almost independent of D_{th}. This is followed by a sudden change (marked by the dotted line) in the slopes of the boundaries marking the transit from a light cone to balloon-shaped OTOC. The boundaries of these late-time balloon shapes are significantly different for different D_{th}. The inset plots of the IS (slope of the boundaries), computed from Eq. (6), show the existence of a constant speed (marked by the dotted line) up to $\tau \approx 204$ after which a change in slope occurs indicating nonballistic behavior of the OTOC. Parameters used are $\{\bar{f} = 0.24, \bar{\gamma} = 0.15, \bar{\kappa} = 1.0\}$.
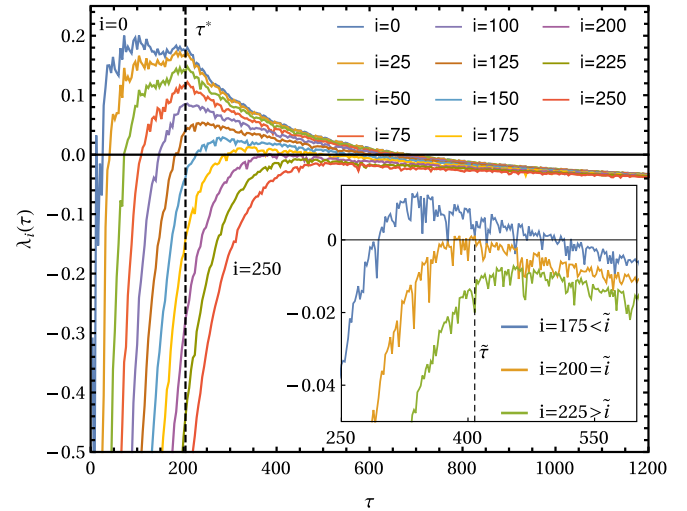

FIG. 11. *FTLE vs time in transient chaos regime:* Initially the FTLE $\lambda_i(\tau) < 0 \, \forall i$. With time, the FTLEs for some oscillators (e.g., $i = 0, 50, 100$) become positive (indicating chaos), whereas $\lambda_i(\tau)$ for $i = 225, 250$, etc., always remain negative (strictly nonchaotic). But the increase in $\lambda_i(\tau)$ for many chaotic oscillators (from $i = 0$ to $i = 100$ in this figure) stops near $\tau \approx 204$ and suffers a *sudden simultaneous* decrease (marked by the dotted line); this is the same point at which a change of slope in the light cone and IS is observed in Fig. 10. Finally, $\lambda_i(\tau)$ for all the oscillators (both transiently chaotic and nonchaotic) saturate to the negative constant $\lambda = -0.06$ indicating long-time nonchaotic behavior. Inset: we show the FTLE for the last oscillator $(\tilde{i})$ that obtains a positive value. Oscillators further than that (i.e., $i > \tilde{i}$) never obtain a positive FTLE. Parameters used are $\{\bar{f} = 0.24, \bar{\gamma} = 0.15, \bar{\kappa} = 1.0\}$.

careful analysis of the boundary of the heat map. In Fig. 10 we plot this boundary for different D_{th} values. Within the light-cone-like structure ($\tau < \tau^*$), boundaries seem to converge for $D_{th} \to 0$. However, for $\tau > \tau^*$, the boundaries depend on D_{th}, although their qualitative features remain same (see Fig. 10). It is interesting to note that while $\tilde{\tau}$ is dependent on D_{th}, τ^* is not. The existence and meaning of $\tilde{\tau}(D_{th})$ can be understood best from the study of FTLEs which we provide in the next paragraph. It is worth mentioning that these boundary features can be equivalently demonstrated by plotting IS versus τ for different D_{th} obtained from Eq. (6) as shown in the inset of Fig 10. Note that the IS starts decreasing with time after $\tau = \tau^*$.

To investigate the reason behind this sudden change in the slope as well as IS, we plot FTLEs for different i as a function of τ in Fig. 11 for $D_{th} = 1$. We observe that for $\tau < \tau^*$, the FTLE for all the oscillators starts increasing with time. Oscillators which are within the light cone achieve positive values for the FTLE by this time. Remarkably, at $\tau = \tau^*$, the FTLE of all these oscillators simultaneously starts decreasing. This is manifested by the sharp corner at $\tau = \tau^*$ of the heat map [see Fig. 1(c)]. Consequently, after this time the rate of spreading of the heat map starts decreasing, and at $\tau = \tilde{\tau}(D_{th})$ it stops spreading as mentioned earlier. For a chosen D_{th} there exists an oscillator $\tilde{i}(D_{th})$ whose FTLE barely touches zero from below at time $\tilde{\tau}(D_{th})$ and remains negative after $\tilde{\tau}(D_{th})$

as shown in the inset of Fig. 11 for $D_{th} = 1$ where $|\tilde{i}(1)| = 200$. The oscillators with index $|i| > |\tilde{i}(D_{th})|$ never achieve a positive FTLE, suggesting that these oscillators never gain the initial perturbation given at the middle (0th) oscillator.

Once we cross the timescale $\tilde{\tau}$ the system starts behaving like a nonchaotic regime, which can be effectively described by a driven dissipative HC. To demonstrate this we compute the OTOC on a driven dissipative HC starting with initial condition $\{y_i(0), \dot{y}_i(0)\}$ taken from the position and velocity configurations of the original nonlinear DC at a time $\tau > \tilde{\tau}$. In Fig. 12 we observe good agreement between the OTOC of the original system with that obtained from the effective driven dissipative harmonic system.

More precisely, we compute the OTOC using following two dynamics: (1) original evolution given in Eq. (3) corresponding to on-site double-well potential $V(x_i) = (-\frac{x_i^2}{2} + \frac{x_i^4}{4}) \, \forall i$ and (2) evolution obtained by performing harmonic approximation of the double-well potential for each oscillator around one of the wells in which the oscillator is at some large time τ, in the original dynamics. If $\{y_i(\tau)\}$ are the positions of the oscillators in the dynamics (i) at time τ, then in the dynamics (ii) we approximate the double potential by $\tilde{V}(y_i) \approx -\frac{1}{2} + (y_i - \delta_i)^2$ where $\delta_i = 1$ if $y_i(\tau)$ falls in the well on the positive side and -1 otherwise. The heat maps corresponding to these two dynamics are shown in Figs. 12(a) and 12(b) from $\tau = 600$ to $\tau = 800$. We observe that these two plots resemble each other quite closely, implying that
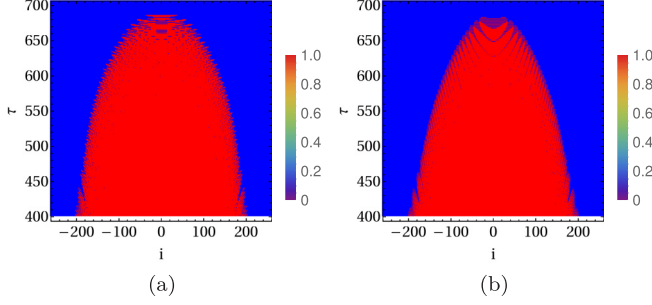
FIG. 12. Comparison of OTOC heat maps in the transient chaos regime obtained from (a) the original dynamics in Eq. (3) with on-site double-well potential and (b) the dynamics in Eq. (14) with harmonic approximation of the double-well potential. Parameters used are $\{\bar{f} = 0.24, \bar{\gamma} = 0.15, \bar{\kappa} = 1.0\}$.

after a large time the oscillators enter from the transiently chaotic to nonchaotic region where the DC effectively behaves like a driven dissipative HC.

Until now we have observed that in this case, the DC dynamics crosses over from a chaotic regime to a nonchaotic regime through a transient regime as demonstrated in the evolution of the FTLE and heat map plot.

We now investigate how this crossover gets manifested through the VDLE. Following the same procedure as done in the previous two sections, we compute the VDLE in the two regimes $\tau < \tau^*$ and $\tau > \tilde{\tau}$.

In Fig. 13 we have plotted $\lambda(v)$ versus v for $\tau \leqslant \tau^*$. For reasons already discussed in Sec. III A for the sustained chaos case, we first try to fit the function $\lambda[1 - (\frac{v}{v_b})^\nu]$ to the VDLE curve in Fig. 13. It is observed that the data around $v \simeq v_b$ fit
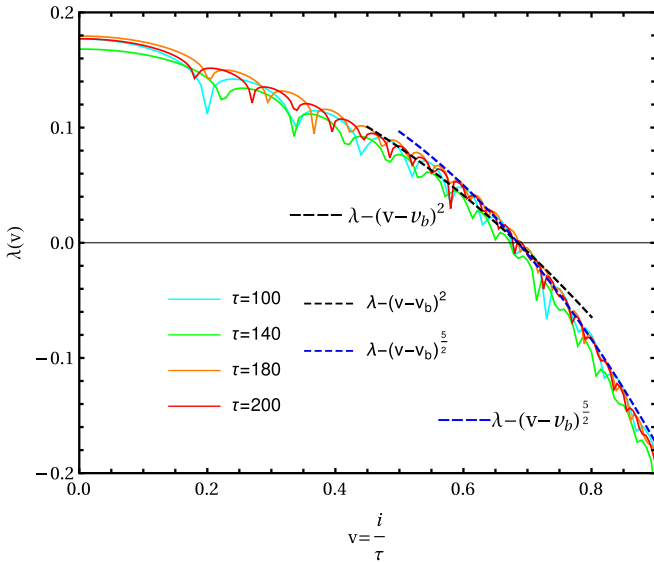

FIG. 13. *VDLE vs v for $\tau < \tau^*$ in the transient chaos regime:* At comparatively short time ($\tau \approx 204$) up to which the light cone exists (marked by the dotted lines in Fig. 10 and Fig. 11), the DC behaves chaotically and the VDLE falls as $\lambda(v) = \lambda(1 - (\frac{v}{v_b})^\nu)$ with $\nu = 2$ and $\nu = \frac{5}{2}$ for $v \leqslant v_b$ and $v \geqslant v_b$, respectively. This is similar to the $\lambda(v)$ behavior in the sustained chaos regime as observed in Fig. 4. Parameters used are $\{\bar{f} = 0.24, \bar{\gamma} = 0.15, \bar{\kappa} = 1.0\}$.
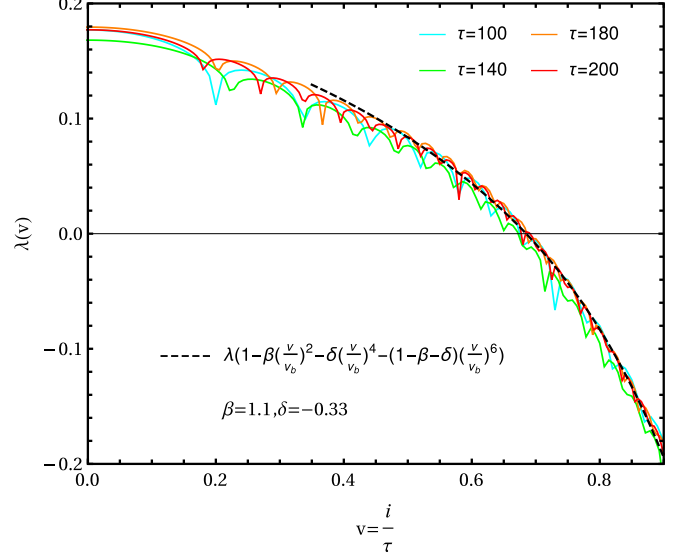

FIG. 14. *VDLE vs v for $\tau < \tau^*$ in the transient chaos regime fitted over a wider range:* At comparatively short time ($\tau \approx 204$) up to which the light cone exists (marked by the dotted lines in Fig. 10 and Fig. 11), the DC behaves chaotically and the VDLE falls in the same way $\lambda(v) = \lambda[1 - \beta(v/v_b)^2 - \delta(v/v_b)^4 - (1 - \beta - \delta)(v/v_b)^6]$ with $\beta = 1.10$ and $\delta = -0.33$ for both inside and outside the light cone near $v \approx v_b$. This is similar to the $\lambda(v)$ behavior in the sustained chaos regime as observed in Fig. 6. Parameters used are $\{\bar{f} = 0.24, \bar{\gamma} = 0.15, \bar{\kappa} = 1.0\}$.

well with the following exponents as follows:

$$\lambda(v) = \begin{cases} \lambda[1 - (v/v_b)^2], & \text{for } v \lesssim v_b \\ \lambda[1 - (v/v_b)^{5/2}], & \text{for } v \gtrsim v_b \end{cases}. \quad (18)$$

A subsequent search for a single functional form of the VDLE that holds for both $v < v_b$ and $v > v_b$ reveals that

$$\lambda(v) = \lambda[1 - \beta(v/v_b)^2 - \delta(v/v_b)^4 - (1 - \beta - \delta)(v/v_b)^6],$$
$$\beta = 1.10, \quad \delta = -0.33, \quad (19)$$

near $v \approx v_b$, which is presented in Fig. 14. On the other hand, for $\tau > \tilde{\tau}$, we observe in Fig. 15 that the data around $v \simeq v_b$ fit well with the following form:

$$\lambda(v) = \begin{cases} \lambda, & \text{for } v \lesssim v_b \\ \lambda - (v - v_b)^{\frac{3}{2}}, & \text{for } v \gtrsim v_b \end{cases}. \quad (20)$$

This is expected since the system has made a transit from the chaotic to nonchaotic regime so that the VDLE here in Eq. (20) behaves in the same way as obtained in Eq. (13) for the nonchaotic scenario.

IV. VARIATION OF FTLE AND IS WITH $\bar{f}$, $\bar{\gamma}$, $\bar{\kappa}$

So far, we have chosen parameters such that we are in a particular regime of interest such as chaotic, nonchaotic, or transient regimes. In this section we study what happens if we tune parameters so that we go through all the regimes. In particular we vary $\bar{f}$ or $\bar{\gamma}$ or $\bar{\kappa}$ continuously and observe how the FTLE [$\lambda_i(\tau)$] or IS [$v_b(\tau, D_{\text{th}})$] changes as we cross from one regime to another. Such studies are important in diverse areas such as optimal signal transmissions, secure
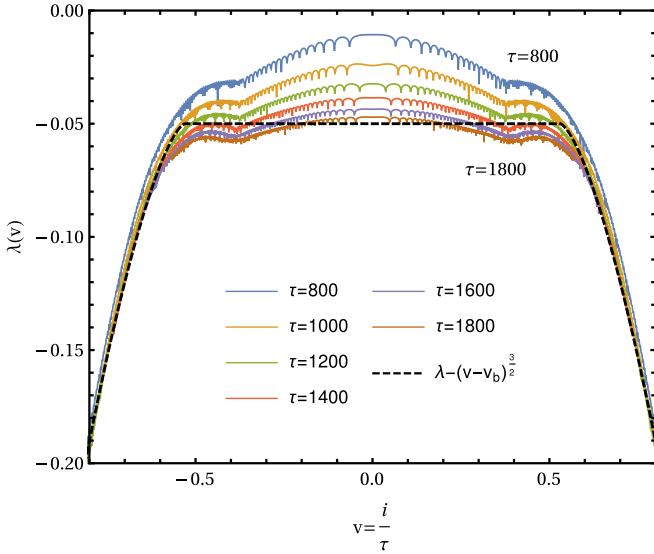
FIG. 15. *VDLE vs v for $\tau \gg \tilde{\tau}$ in the transient chaos regime:* At large time ($\tau \geqslant 800$), the VDLE is negative meaning the whole DC becomes nonchaotic. Here the VDLEs satisfy the relation $(\lambda(v) - \lambda) \sim -(v - v_b)^{3/2}$ for $v \geqslant v_b$. This is consistent with the $\lambda(v)$ behavior in the nonchaotic regime as observed in Fig. 9. Parameters used are $\{\bar{f} = 0.24, \bar{\gamma} = 0.15, \bar{\kappa} = 1.0\}$.

communications, and synchronization in electronic circuits [86–90], where a common goal is to gain control over chaotic systems. In this connection, we should mention that a novel chaotic secure communication system has been proposed in Ref. [75] where the encryption system consists of a Duffing oscillator. However, it is also argued [75] that use of only one Duffing oscillator in the encryption stage leads to low level of security. So one might think of considering the coupled DC as a plausible candidate for increasing the security level of the encrypted messages in those communication systems.

For FTLE measurement we choose to study $\lambda_0(\tau)$, and for $v_b(\tau, D_{th})$ we fix $D_{th} = 1$. Note again that $v_b(\tau, 1)$ in different regimes behaves as

$$v_b(\tau, 1) \begin{cases} = 0, & \text{for large } \tau \Rightarrow \text{Nonchaotic} \\ = v_b > 0, & \text{for large } \tau \Rightarrow \text{Sustained chaos} \\ \left.\begin{array}{l} > 0 \text{ for small } \tau \\ = 0 \text{ for large } \tau \end{array}\right\} \Rightarrow \text{Transient chaos.} \end{cases} \quad (21)$$

On the other hand, for different choices of parameters we look at the saturation value $\lambda = \lambda_0(\tau)|_{\tau \to \infty}$ to check if the DC belongs to sustained chaos ($\lambda > 0$) or nonchaotic ($\lambda < 0$) regimes. In Figs. 16(a) and 16(b), we present heat map plots of λ in the $\bar{\gamma} - \bar{f}$ plane at $\tau = 300$ and $\tau = 1200$, respectively, for $\bar{\kappa} = 1$. In both plots, the red (light gray) regions correspond to sustained chaos regime, and the blue (dark) regions correspond to the nonchaotic regime. When comparing between Figs. 16(a) and 16(b), a careful observation reveals the disappearance of red (light gray) regions (and appearance of blue (dark) regions accordingly) when going from Fig. 16(a)($\tau = 300$) to Fig. 16(b) ($\tau = 1200$), indicating the existence of transient chaos regimes. To identify these
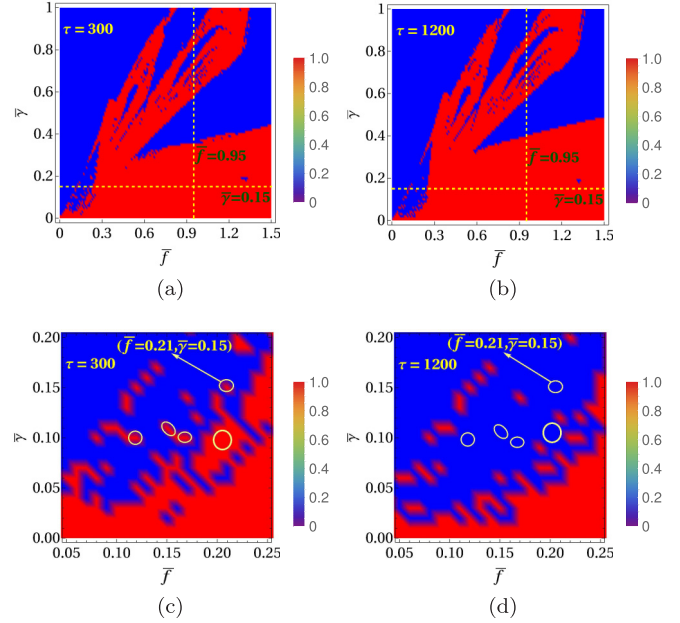

FIG. 16. *Identifying different dynamical regimes of the DC in the $\bar{f} - \bar{\gamma}$ parameter plane:* The heat maps in (a) and (b) show the dynamical behavior of the DC in $\bar{\gamma} - \bar{f}$ plane as we vary $\bar{f} \in [0, 1.5]$ and $\bar{\gamma} \in [0, 1]$ at time $\tau = 300$ (left panel) and $\tau = 1200$ (right panel), respectively. The parameter regime with large drive and comparatively small dissipation (e.g., $\bar{f} \in [0.5, 1.5]$) and $\bar{\gamma} \in [0, 0.3]$) is spanned by sustained chaos [red (light gray) region], whereas the parameter regime corresponding to low drive and large dissipation (e.g., $\bar{f} \in [0, 0.2]$ and $\bar{\gamma} \in [0.3, 1]$) results in a fully nonchaotic regime [blue (dark) region]. These fully chaotic and fully nonchaotic regions are separated by regions of highly intermittent dynamical behaviors; for example, in $(\bar{f}, \bar{\gamma}) \in [0.5, 1]$, we observe a mixture of puddles of chaotic and nonchaotic windows [irregularly occurring red (light gray) and blue (dark) regions[. The DC dynamics along the dashed lines $\bar{\gamma} = 0.15$ and $\bar{f} = 0.95$ is discussed in detail. To identify the transient chaos regions, in panels (c) and (d), we plot zoomed-in portions of (a) and (b), respectively. As we shift from the left panel ($\tau = 300$) to the right panel ($\tau = 1200$), we observe the disappearance of the previously existing transient chaos regions. Some of these transient chaos regions are enclosed by yellow rings, which appear as chaotic [red (light gray)] at $\tau = 300$ but become nonchaotic [blue (dark)] at $\tau = 1200$. One such particular parameter set ($\bar{f} = 0.21, \bar{\gamma} = 0.15$) corresponding to transient chaos is pointed out in both panels and will be discussed more elaborately in the next section. Here the coupling constant is fixed at $\bar{\kappa} = 1.0$.

transient chaos regions more appropriately, we zoom in a particular parameter region from Figs. 16(a) and 16(b) and plot them in Figs. 16(c) and 16(d), respectively. There we observe that the regions marked by yellow rings are red (light gray) at an earlier time ($\tau = 300$, left panel), whereas they become blue (dark) at a later time ($\tau = 1200$, right panel), implying that these parameter regions correspond to transient chaos regimes.

In the sections below we discuss, in detail, our numerical results for the variation of $\lambda_0(\tau)$ and $v_b(\tau, 1)$ with respect to one parameter (while keeping the other two fixed) for different times τ.
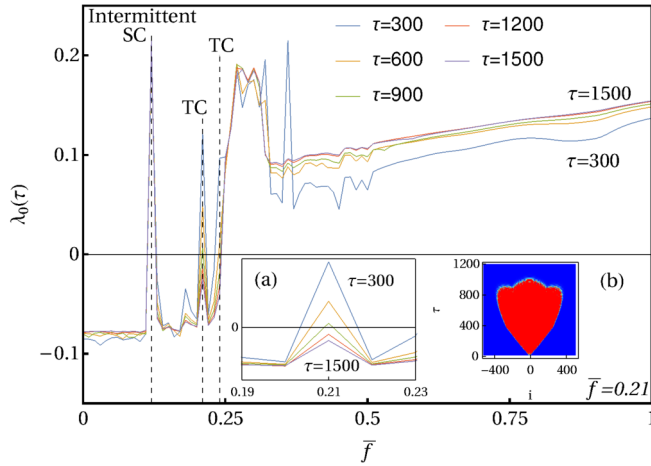
FIG. 17. *FTLE vs $\bar{f}$:* The driving amplitude value $\bar{f}^* = 0.25$ separates the sustained chaos (SC) regime ($\bar{f} > 0.25$) from the nonchaotic (NC) regime ($0 < \bar{f} < 0.25$). In $\bar{f} > 0.25$ (SC), the FTLE curves at large times saturate to constant $\lambda > 0$, whereas the curves in $0 < \bar{f} < 0.25$ (NC) saturate to $\lambda < 0$. Particularly, deep inside the SC regime, for $0.35 < \bar{f} < 1$, $\lambda_0(\tau)$ is a monotonically increasing function of $\bar{f}$. Inside the NC regime, we note that there exists an intermittent chaotic window at $\bar{f} = 0.12$ and a few transient chaos points, e.g., at $\bar{f} = 0.21$ and $\bar{f} = 0.24$ [(heat map in Fig. 1(c)] characterized by the crossing of $\lambda_0(\tau)$ from positive to negative values as time progresses. The transient behavior at $\bar{f} = 0.21$ is zoomed in the inset (a) where we observe that $\lambda_0(\tau)$ transits from a positive value to a negative value as time increases. This transient behavior is also seen from the heat map presented in inset (b). In all plots, the measurements are performed after every $\Delta \bar{f} = 0.01$ on the x axis. Parameters used are $\{\bar{\gamma} = 0.15, \bar{\kappa} = 1.0\}$.

A. Variation with respect to $\bar{f}$

In Fig. 17 and Fig. 18 we plot the variation of $\lambda_0(\tau)$ and $v_b(\tau, 1)$ with respect to $\bar{f}$, respectively, for $\bar{\gamma} = 0.15$, $\bar{\kappa} = 1.0$, and different values of τ. In both plots we observe that with $\bar{f}$, increasing from 0 to 1, the system crosses over from nonchaotic to sustained chaos regime through an intermediate transient regime [$\bar{f} \sim (0.21–0.24)$]. However, deep inside the nonchaotic regime we observe some intermittent window of sustained chaos ($\bar{f} = 0.12$).

Although both the FTLE and IS are time-dependent entities in general, the convergence of the curves at large times clearly indicates the parameter regions giving rise to a sustained chaos regime or nonchaotic regime as can be observed in Fig. 17 and Fig. 18. In particular we observe in Fig. 17 that $\bar{f}^* = 0.25$ separates the sustained chaos ($\bar{f} > 0.25$) regime with $\lambda_0(\tau \to \infty) = \lambda > 0$ and the nonchaotic regine ($0 < \bar{f} < 0.25$) with $\lambda_0(\tau \to \infty) = \lambda < 0$. The same sustained chaos and nonchaotic regimes can be alternatively identified from Fig. 18 with $v_b(\tau, 1) = v_b > 0$ and $v_b(\tau, 1) = v_b = 0$, respectively.

As mentioned earlier, inside the nonchaotic region $0 < \bar{f} < \bar{f}^*$, we interestingly observe intermittent points of sustained chaos (e.g., at $\bar{f} = 0.12$) and transient chaos (e.g., at $\bar{f} = 0.21$ and $\bar{f} = 0.24$). The appearance of transient chaos at $\bar{f} = 0.24$ has already been discussed in Sec. III C. Here
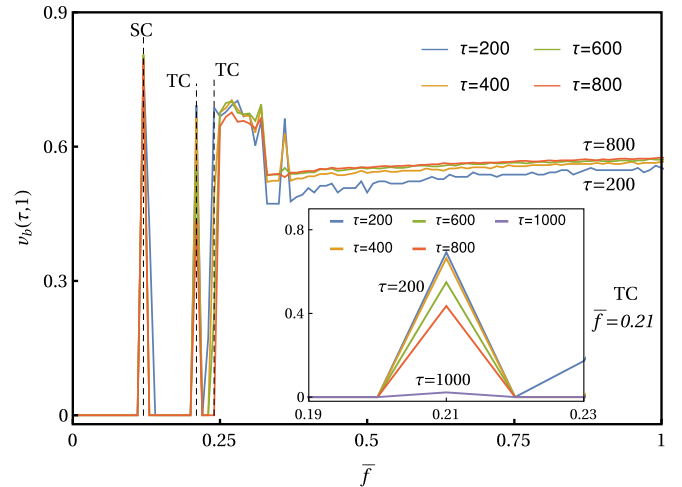

FIG. 18. *IS vs $\bar{f}$:* The IS characterizes the nonchaotic (NC) regime ($0 < \bar{f} < 0.25$) with $v_b(\tau) = 0$, whereas the IS curves at different times saturate to constant $v_b(\tau) = v_b > 0$ in sustained chaos (SC) regime ($\bar{f} > 0.25$). Inside the SC regime, for $0.4 < \bar{f} < 1.0$, IS is a monotonically increasing but much slowly varying function of $\bar{f}$ in comparison to FTLE. Inside the NC regime ($0 < \bar{f} < 0.25$), the transient chaos points $\bar{f} = 0.21$ and $\bar{f} = 0.24$ are characterized by a decreasing $v_b(\tau)$ to zero as time progresses. This decrease is shown for $\bar{f} = 0.21$ in the inset. The intermittent chaotic window appears at $\bar{f} = 0.12$, and it has also been observed in Fig. 17. At this point, we also observe that $v_b(\tau) = v_b > 0$. In all plots, the measurements are performed after every $\Delta \bar{f} = 0.01$ on the x axis. Parameters used are $\{\bar{\gamma} = 0.15, \bar{\kappa} = 1.0\}$.

we focus on the transient chaos appearing at $\bar{f} = 0.21$ and demonstrate how one can identify this feature from the $\lambda(\tau)$ versus $\bar{f}$ and $v_b(\tau)$ versus $\bar{f}$ plots for different τ. In Fig. 17(a) we zoom the behavior of $\lambda_0(\tau)$ near $\bar{f} = 0.21$ where we note that at smaller τ, the FTLE $\lambda_0(\tau) > 0$, suggesting the dynamics could be chaotic. But with increasing τ, we observe that the value of the FTLE at $\bar{f} = 0.21$ decreases, and finally at large τ it saturates to a value $\lambda < 0$. This indicates that the dynamics for $\bar{f} = 0.21$ is actually transient, which crosses over from sustained to nonchaotic regime as time progresses. For reference, a heat map plot of the OTOC at $\bar{f} = 0.21$ is also shown in Fig. 17(b). Alternatively, the same feature at this value of $\bar{f}$ can be observed from the $v_b(\tau, 1)$ versus $\bar{f}$ plots for different values of τ in Fig. 18, where the crossover is demonstrated (see the inset of Fig. 18) by the decrease of IS to zero with increasing τ as shown in Eq. (21).

Deep inside the SC regime, for $\bar{f} \in [0.4, 1]$, we observe that FTLE grows linearly with $\bar{f}$ for large $\bar{f}$. In connection to this observation, it is worth mentioning a recent conjecture $\lambda \propto \sqrt{T}$ made for a classical chaotic Hamiltonian systems where T is the temperature [39]. Our observation $\lambda \propto \bar{f}$ in Fig. 17 is similar in spirit with this conjecture as the energy scale of each oscillator in the SC regime is $\sim \bar{f}^2$, which can be considered as effective temperature in our driven dissipative system. On the other hand, as observed in Fig. 18, $v_b(\tau, 1)$ almost remain constant as we vary $\bar{f}$ inside the SC regime. This indicates that the driving amplitude ($\bar{f}$) has more impact on the FTLE than on IS.
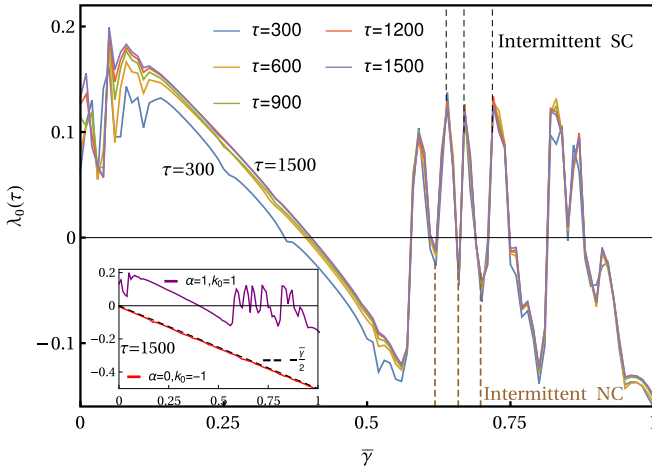
FIG. 19. *FTLE vs $\bar{\gamma}$:* The dissipation value $\bar{\gamma}^* = 0.4$ separates the sustained chaos (SC) regime ($0 < \bar{\gamma} < 0.4$) from the nonchaotic (NC) regime ($\bar{\gamma} > 0.4$). In $0.05 < \bar{\gamma} < 0.55$, the FTLE is a monotonically decreasing function of $\bar{\gamma}$. The FTLE curves at different τ saturate to $\lambda_0(\tau) = \lambda > 0$ in the SC regime and to $\lambda_0(\tau) = \lambda < 0$ in the NC regime. The parameter regime $0.55 < \bar{\gamma} < 0.85$ (inside the NC regime) exhibits a highly intermittent behavior with several chaotic windows. To understand the importance of nonlinearity, in the inset we compare the dependence of the FTLE saturation value on $\bar{\gamma}$ (as shown in the main plot) with that of a driven dissipative HC. For the latter we observe that the FTLE saturates to $-\bar{\gamma}/2$ for $\bar{\gamma} > 0$. The measurements are taken with the resolution $\Delta\bar{\gamma} = 0.01$ along the x axis. Parameters used are $\{\bar{f} = 0.95, \bar{\kappa} = 1.0\}$.

B. Variation with respect to $\bar{\gamma}$

In this section we study the variation of $\lambda_0(\tau)$ and $v_b(\tau, 1)$ with respect to $\bar{\gamma}$ for $\bar{f} = 0.95$ and $\bar{\kappa} = 1.0$ at different values of τ. In Fig. 19 and Fig. 20 we plot the variation of $\lambda_0(\tau)$ and $v_b(\tau, 1)$, respectively, over the range $\bar{\gamma} \in [0, 1]$. As noticed earlier, the curves at large τ converge in both figures. We
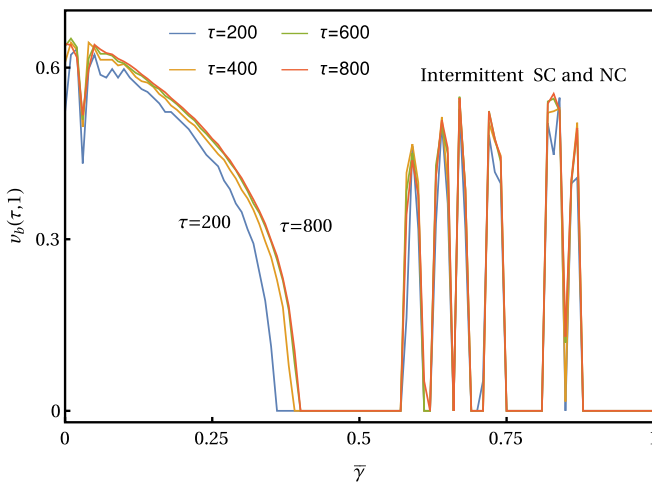

FIG. 20. *IS vs $\bar{\gamma}$:* In the SC regime ($0 < \bar{\gamma} < 0.4$), $v_b(\tau)$ curves for different τ saturate to $v_b(\tau) = v_b > 0$ and behave in a monotonically decreasing way as $\bar{\gamma}$ is increased. Inside the NC regime ($0.4 < \bar{\gamma} < 1$), the intermittent chaotic windows have $v_b(\tau) = v_b > 0$ surrounded by all NC points with $v_b(\tau) = v_b = 0$. Parameters used are $\{\bar{f} = 0.95, \bar{\kappa} = 1.0\}$.
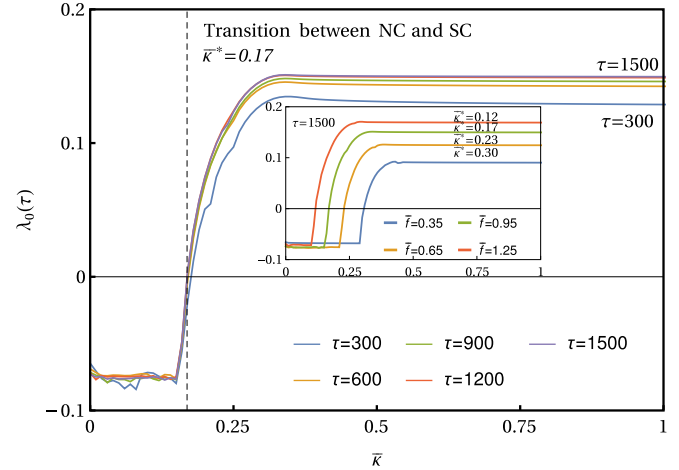

FIG. 21. *FTLE vs $\bar{\kappa}$:* For $\kappa = 0$, $\lambda_0(\tau) = \lambda < 0$ implies the uncoupled DC is nonchaotic. As the coupling is turned on and increased, the DC becomes chaotic at $\bar{\kappa}^* = 0.17$. In the nonchaotic (NC; $0 < \bar{\kappa} < 0.17$) and sustained chaos (SC; $\bar{\kappa} > 0.17$) regimes the FTLE curves at different τ saturate to $\lambda_0(\tau \to \infty) = \lambda < 0$ and $\lambda_0(\tau \to \infty) = \lambda > 0$, respectively. It is also observed that deep inside the SC and NC regimes, $\lambda_0(\tau \to \infty)$ is a very slowly varying function of $\bar{\kappa}$. In the inset ($\bar{\gamma} = 0.15$, $\tau = 1500$), we observe that with increasing driving amplitude ($\bar{f}$), the minimum coupling ($\bar{\kappa}^*$) required to make the DC chaotic decreases. Parameters used are $\{\bar{f} = 0.95, \bar{\gamma} = 0.15\}$ for the main figure.

see that the value $\bar{\gamma}^* = 0.4$ marks the transition from the SC regime [$\bar{\gamma} \in (0, 0.4)$] to the NC regime [$\bar{\gamma} \in (0.4, 1.0)$]. It seems that the FTLE in Fig. 19 decreases approximately linearly with increasing $\bar{\gamma}$ in the regime $0.05 < \bar{\gamma} < 0.55$. This sustained chaos regime is identified by a monotonic but nonlinear decrease of $v_b(\tau, 1)$ with increasing $\bar{\gamma}$ in Fig. 20. It is interesting to observe that this monotonic decrease in the FTLE and IS is followed by a highly intermittent behavior as we further increase the dissipation [$\bar{\gamma} \in (0.55, 1)$]. In particular, we observe a mixture of chaotic and nonchaotic windows in this parameter regime from both Fig. 19 and Fig. 20.

To understand the above mentioned approximately linear decrease of the FTLE for $0.05 < \bar{\gamma} < 0.55$, we look at how FTLE $\lambda_0(\tau)$ varies with increasing $\bar{\gamma}$ for a driven dissipative HC. For this case it is possible to compute the FTLE analytically (see Appendix A), and we find $\lambda_0(\tau)$ decays linearly as $\lambda_0(\tau) = -\frac{\bar{\gamma}}{2}$. In the inset of Fig. 19, a comparison between the FTLE of the HC and of the DC is provided. We observe that the FTLE in the anharmonic case decays with $\bar{\gamma}$, although the dynamics at small $\bar{\gamma}$ is chaotic in contrast to the harmonic case for which the dynamics is always nonchaotic as expected. However, upon increasing $\bar{\gamma}$ further the FTLE goes beyond zero and becomes negative till $\bar{\gamma} = 0.56$ after which the behavior with respect to $\bar{\gamma}$ becomes irregular with chaotic and nonchaotic regimes appearing apparently abruptly.

C. Variation with respect to $\bar{\kappa}$

Here we would like to discuss the effect of the coupling ($\bar{\kappa}$) on $\lambda_0(\tau)$ and $v_b(\tau, 1)$ at different τ, while the other parameters are fixed to $\bar{f} = 0.95$, $\bar{\gamma} = 0.15$. From Fig. 21 and Fig. 22, we note that when $\bar{\kappa} = 0$, i.e., for uncoupled Duffing oscillators,
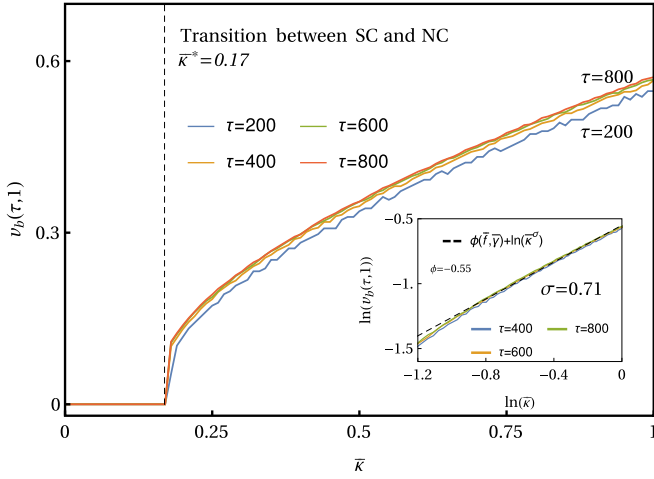
FIG. 22. *IS vs $\bar{\kappa}$:* In the sustained chaos (SC) $(0.17 < \bar{\kappa} < 1)$ regime, the IS curves at different τ converge to $v_b(\tau, 1) = v_b > 0$, whereas we see $v_b(\tau, 1) = v_b = 0$ in the nonchaotic (NC) $(0 < \bar{\kappa} < 0.17)$ regime. Inside the SC regime, for comparatively large κ ($\kappa > 0.4$), the IS varies with $\bar{\kappa}$ as $v_b \sim \kappa^\sigma$ with $\sigma = 0.71$. That $\sigma = 0.71$ is shown in the inset by plotting the main figure in log-log scale. Parameters used are $\{\bar{f} = 0.95, \bar{\gamma} = 0.15\}$.

the system is nonchaotic with $\lambda_0(\tau) = \lambda < 0$ and $v_b(\tau, 1) = 0$, respectively.

In Fig. 21 it is very interesting to observe, as we turn on the coupling $\bar{\kappa}$, that near $\bar{\kappa}^* = 0.17$, the DC transits from the nonchaotic $[\lambda_0(\tau) = \lambda < 0]$ to the sustained chaos regime $[\lambda_0(\tau) = \lambda > 0]$. Equivalently, this feature manifests itself as a transition from $v_b(\tau, 1) = v_b < 0$ to $v_b(\tau, 1) = v_b > 0$ in Fig. 22. So this behavior of the DC indicates that coupling alone can initiate chaos in spatially extended systems. To understand the difference between the dynamics of the uncoupled and coupled Duffing oscillators in the sustained chaos, transient chaos, and nonchaotic regimes explicitly, a brief discussion comparing the corresponding dynamical behaviors using the FTLE is presented in Appendix B.

A natural question one might ask is, How does the minimum coupling strength $\bar{\kappa}^*$, required to make the system chaotic, change as we vary the driving amplitude $\bar{f}$? This is an important question given the possibility of tuneability of various parameters such as coupling and driving. To answer this, we present the behavior of $\lambda_0(\tau)$ versus $\bar{\kappa}$ for different values of $\bar{f}$ at large time in the inset of Fig. 21. We observe that as we increase the driving amplitude $\bar{f}$, $\bar{\kappa}^*$ decreases, which implies at higher $\bar{f}$ comparatively lower coupling is sufficient to turn on the chaos in the DC. However, for $\bar{\kappa} \in (0.35, 1)$, i.e., deep inside the chaotic regime, and $\bar{\kappa} \in (0, 0.15)$, i.e., deep inside the nonchaotic regime, we observe from Fig. 21 that the FTLE is almost independent of $\bar{\kappa}$ as manifested by plateau regions on the right and left of the $\bar{\kappa}^*$.

On the other hand, in the sustained chaos regime corresponding to the range $0.17 < \bar{\kappa} < 1.0$, from Fig. 22 we see that $v_b(\tau, 1)$ increases significantly with $\bar{\kappa}$ as a power law. In this regard, one may note that even in the absence of nonlinearity (a driven dissipative HC), v_b behaves as a power law $v_b \sim \sqrt{\kappa}$ (see Appendix A). In the presence of nonlinearity, as shown in the inset of Fig. 22, it is interesting to observe

that deep inside the sustained chaos regime, corresponding to $\bar{\kappa} \in (0.4, 1)$, at large time, the IS follows the functional form $v_b \sim \kappa^\sigma$ with $\sigma = 0.71$. The fact that σ is different from 0.5 is a fingerprint of nonlinearity, which explicitly includes the effect of drive strength in contrast to the HC case.

V. CONCLUSIONS AND OUTLOOK

In this paper, we have studied the dynamics of a driven dissipative chain of coupled Duffing oscillators. Interestingly, depending on the choice of the system parameters (namely, the driving amplitude, driving frequency, dissipation, nonlinearity, and coupling strength), the DC is observed to exhibit rich dynamical behavior with three different dynamical regimes: (1) sustained chaos, (2) nonchaotic regime, and (3) transient chaos. Although the existence of these dynamical regimes was known [80], powerful diagnostics to investigate these rich regimes have been missing.

We have thoroughly investigated these dynamical regimes by introducing the out-of-time-ordered correlator (OTOC) as a promising tool which serves as a measure of both the spatial spread and temporal growth (or decay) of an initially localized infinitesimal perturbation. We have observed that spatiotemporal heat maps of the OTOC (Fig. 1) clearly demonstrate the existence of the different dynamical regimes. While the OTOC grows exponentially in the sustained chaos regime, it decays in the nonchaotic regime. In the transient regime we have found that the OTOC at small times looks like the sustained chaos pattern, but at large time it crosses over to the nonchaotic regime, where it ceases both to grow exponentially and spread ballistically.

In order to quantify separately the spatial spread and and temporal growth (or decay) of the OTOC, we have looked at the instantaneous speed [IS, Eq. (6)] and the finite-time Lyapunov exponent [FTLE, Eq. (7)], defined directly from the OTOC. Equivalently, to characterize the temporal growth (or decay) of perturbation in a frame moving with a velocity (v) with respect to the initially perturbed oscillator, we have used the velocity-dependent Lyapunov exponent [VDLE, $\lambda(v)$] as a spatiotemporal measure of the dynamics, defined directly from the OTOC in Eq. (10). Through extensive numerical simulation and theoretical arguments, we show that these quantities characterize the above mentioned regimes very well.

We have shown that for all three regimes the FTLE starts from a value <0 initially and finally saturates to a nonzero value. For sustained chaos we find that the FTLE saturates to a $\lambda > 0$, thus crossing the $\lambda = 0$ value only once, whereas for the nonchaotic case it never becomes positive and saturates, at large time, to a negative value. In the case of the transient chaos regime, the FTLE for some oscillators, starting from a negative value, increases to a positive value, and at a certain time, the FTLEs of all these oscillators start decreasing simultaneously and finally, at large time, saturate to a negative value. Thus in this regime the FTLE crosses the $\lambda = 0$ line twice. We also have shown that IS also provides a good diagnostic for the detection of the three regimes. In particular, we have found that the VDLE in the three regimes behaves distinctly in the sustained regime and in the nonchaotic regime, whereas in the transient regime, as for the other two diagnostics, it shows behaviors similar to sustained chaos at small

times and behaviors similar to nonchaotic regimes at late times. All these features are summarized in Table I.

We have also studied the behavior of the FTLE and IS when the driving amplitude ($\bar{f}$), dissipation ($\bar{\gamma}$), and coupling strength ($\bar{\kappa}$) are changed separately. Such studies are particularly important in the context of gaining control and tuneability over chaotic systems. In all three cases, we find that typically the sustained chaos regime and the nonchaotic regimes are separated by a transient chaos regime with intermittent sustained chaos points appearing inside the nonchaotic regime. When $\bar{f}$ is increased from a small value the DC undergoes a transition from the nonchaotic to sustained chaos regime (see Fig. 17 and Fig. 18). Deep inside the sustained chaos regime, interestingly, the saturated FTLE increases linearly with $\bar{f}$ (Fig. 17). Similar observations are made from the variation of IS with changing $\bar{f}$ as well, the only difference being that the IS does not change much with the increasing drive deep inside the chaotic region. On the other hand, we have observed a monotonic and linear decrease in the FTLE (Fig. 19) and a nonlinear decrease in IS (Fig. 20) with increasing dissipation in the sustained chaos region. This is followed by a highly intermittent mixture of chaotic and periodic windows as one further increases the dissipation. In the case of variation with respect to coupling strength (κ), the most important observation (see Fig. 21) that we made is as follows: by turning the harmonic coupling only, it is possible to make the dynamics of the DC transit from a nonchaotic to chaotic regime, and this happens at a critical strength κ^*, which decreases with increasing driving amplitude. We observe that IS varies with κ as $v_b \sim \kappa^\sigma$ (see Fig. 22). Interestingly, σ for the DC is found to be different from $\frac{1}{2}$ obtained for a driven dissipative HC.

Our work can be explored further in several directions. Since most of our findings rely on extensive numerical simulation, it would be very interesting to explore possible analytical means of describing the numerical results obtained in this work. In particular we feel it would be possible to develop a perturbation theory for capturing the nonchaotic to chaotic crossover. Another interesting direction to explore is the sensitivity to initial conditions [73]. In the present paper, we have dealt with a fixed initial condition. One could investigate the sensitivity of the dynamical properties to different sets of initial conditions. A crucial direction is to investigate the effect of adding a stochastic noise [20] on the dynamical behavior of the driven-dissipative DC. To study the generality of the results obtained here, one can consider different systems like a self-sustained chain of oscillators, e.g., coupled Van der Pol oscillators or coupled Van der Pol–Duffing oscillators [71], to analyze the intricate interplay between the self-sustained characteristic with external drive, dissipation, and coupling. Having a handle on the classical driven dissipative system, it is a fascinating and a challenging task to study the quantum version of these models [91,92].

APPENDIX A: VDLE FOR A DRIVEN DISSIPATIVE LINEAR HARMONIC CHAIN (HC)

In Sec. III B we have discussed that, in the nonchaotic regime, the dynamics of the DC essentially acts as a driven dissipative linear HC. A brief calculation has been demonstrated there for the corresponding behavior of the VDLE in Eq. (13). Here we present a rigorous derivation for the results in Eq. (13) starting from the evolution equation of perturbations [Eq. (14)],

$$\frac{d^2\delta y_i}{d\tau^2} = -k_0 \delta y_i - \bar{\gamma}\frac{d\delta y_i}{d\tau} + \bar{\kappa}(\delta y_{i-1} + \delta y_{i+1} - 2\delta y_i), \text{(A1)}$$

where $1 \leqslant i \leqslant N$. We consider the same initial conditions as in Eq. (9): $\delta y_i = \epsilon \delta_{i,\frac{N+1}{2}}, \frac{d\delta y_i}{d\tau} = 0$ for $i = 1, 2, \ldots, N$. Equation (A1) can be represented in the following matrix form:

$$\frac{d^2\delta\mathbf{Y}}{d\tau^2} = M\delta\mathbf{Y} - \bar{\gamma}\frac{d\delta\mathbf{Y}}{d\tau}, \text{(A2)}$$

where $\delta\mathbf{Y} = (\delta y_1 \ldots \delta y_i \ldots \delta y_N)^T$ and the matrix M is the following $N \times N$ matrix:

$$M = \begin{pmatrix} -2\bar{\kappa} - k_0 & \bar{\kappa} & 0 & 0 .. 0 & \bar{\kappa} \\ \bar{\kappa} & -2\bar{\kappa} - k_0 & \bar{\kappa} & 0 .. 0 & 0 \\ 0 & \bar{\kappa} & -2\bar{\kappa} - k_0 & \bar{\kappa} .. 0 & 0 \\ . & . & . & . .. . & . \\ . & . & . & . .. . & . \\ \bar{\kappa} & 0 & 0 & 0 .. \bar{\kappa} & -2\bar{\kappa} - k_0 \end{pmatrix}. \text{(A3)}$$

The eigenvalues ν_i and eigenvectors $|\psi_i\rangle$ ($i = 1, 2, \ldots, N$) of M are obtained to be

$$\nu_i = -k_0 - 4\bar{\kappa}\,\sin^2\left(\frac{\pi i}{N}\right),$$

$$\psi_i^j = \frac{1}{\sqrt{N}}\left[\cos\left(\frac{2\pi i j}{N}\right) + \sin\left(\frac{2\pi i j}{N}\right)\right], \text{(A4)}$$

with ψ_i^j being the jth component of $|\psi_i\rangle$. Consequently, the matrix in Eq. (A3) can be diagonalized as $M_d = U^{-1}MU$, where $(M_d)_{i,j} = \nu_i\delta_{i,j}$ and $U_{i,j} = \psi_i^j$. Also note that in this case $U_{i,j}^{-1} = U_{i,j} = \psi_i^j$. So Eq. (A2) can now be expressed conveniently as

$$\frac{d^2\delta\mathbf{Q}}{d\tau^2} = M_d\delta\mathbf{Q} - \bar{\gamma}\frac{d\delta\mathbf{Q}}{d\tau}, \text{(A5)}$$

where $\delta\mathbf{Q} = (\delta q_1 \ldots \delta q_i \ldots \delta q_N)^T$ with $\delta q_i = \sum_j U_{i,j}^{-1} \delta y_i$; δq_i are uncoupled variables with individual equations of motions such as

$$\frac{d^2 \delta q_i}{d\tau^2} + \bar{\gamma} \frac{d\delta q_i}{d\tau} - v_i \delta q_i = 0. \tag{A6}$$

The above equation, being uncoupled, can be solved directly, and the resulting solution is given as

$$\delta q_i(\tau) = \epsilon\, e^{\frac{-\bar{\gamma}\tau}{2}} U_{i,\frac{N+1}{2}}^{-1} \left[\cos(\Delta_i \tau) + \frac{\bar{\gamma}}{2\Delta_i} \sin(\Delta_i \tau) \right], \tag{A7}$$

where

$$\Delta_j = \sqrt{4\bar{\kappa} \sin^2\left(\frac{\pi j}{N}\right) + k_0 - \left(\frac{\bar{\gamma}}{2}\right)^2}.$$

We would be dealing with the underdamped scenario where $(\frac{\bar{\gamma}}{2})^2 < k_0$. Now we can invert δq_i to obtain the following expression for $\delta y_i(\tau) = \sum_j U_{i,j} \delta q_i(\tau)$:

$$\delta y_i(\tau) = \frac{\epsilon\, e^{-\frac{\bar{\gamma}\tau}{2}}}{N} \sum_{j=1}^{N} \psi_i^j \psi_j^{\frac{N+1}{2}} \left[\cos(\Delta_j \tau) + \frac{\bar{\gamma}}{2\Delta_j} \sin(\Delta_j \tau) \right]. \tag{A8}$$

By using Eq. (A4) and making a shift in the oscillator index as $i \to (i - \frac{N+1}{2})$, we obtain the OTOC defined as $D(i, \tau) = \frac{\delta y_i}{\epsilon}$, which is given by

$$D(i, \tau) = \frac{e^{-\frac{\bar{\gamma}\tau}{2}}}{N} \sum_{j=1}^{N} \left\{ \cos\left(\frac{2\pi i j}{N}\right) + \sin\left[\frac{2\pi j}{N}(i+1)\right] \right\}$$
$$\times \left[\cos(\Delta_j \tau) + \frac{\bar{\gamma}}{2\Delta_j} \sin(\Delta_j \tau) \right], \tag{A9}$$

for $-\frac{N-1}{2} \leqslant i \leqslant \frac{N-1}{2}$. Now we note that

$$\sum_{j=1}^{N} \sin\left[\frac{2\pi j}{N}(i+1)\right]\left[\cos(\Delta_j \tau) + \frac{\bar{\gamma}}{2\Delta_j} \sin(\Delta_j \tau)\right]$$
$$= \sum_{j=1}^{N} \chi(i, j, \tau) = 0, \tag{A10}$$

using the fact $\chi(i, N - j, \tau) = -\chi(i, j, \tau)$ for $j = 1, 2 \ldots (N-1)/2$ and $\chi(i, N, \tau) = 0$. So, using (A10), Eq. (A9) reduces to

$$D(i, \tau)$$
$$= \frac{e^{-\bar{\gamma}\tau/2}}{N} \sum_{j=1}^{N} \cos\left(\frac{2\pi i j}{N}\right)\left[\cos(\Delta_j \tau) + \frac{\bar{\gamma}}{2\Delta_j} \sin(\Delta_j \tau)\right]$$
$$= \frac{e^{-\frac{\bar{\gamma}\tau}{2}}}{2N} \sum_{j=1}^{N} \left\{ \cos\left(\frac{2\pi i j}{N} - \Delta_j \tau\right) + \cos\left(\frac{2\pi i j}{N} + \Delta_j \tau\right) \right.$$
$$\left. + \frac{\bar{\gamma}}{2\Delta_j}\left[\sin\left(\frac{2\pi i j}{N} + \Delta_j \tau\right) - \sin\left(\frac{2\pi i j}{N} - \Delta_j \tau\right)\right] \right\}. \tag{A11}$$

Using a suitable variable transformation of the form $\tilde{j} = (N - j)$ and some well-known trigonometric identities, it is straightforward to prove that the first two (cos) sums in Eq. (A11) are

equal and the other two remaining (sin) sums are also equal. Consequently, Eq. (A11) simplifies to

$$D(i, \tau) = \frac{e^{-\bar{\gamma}\tau/2}}{N} \times \sum_{j=1}^{N} \left[\cos\left(\frac{2\pi i j}{N} - \Delta_j \tau\right) \right.$$
$$\left. - \frac{\bar{\gamma}}{2\Delta_j} \sin\left(\frac{2\pi i j}{N} - \Delta_j \tau\right) \right]. \tag{A12}$$

Since we are considering a spatially extended system of very large size N, in the limit $N \to \infty$, we can take the continuum limit of Eq. (A11) by identifying $\frac{\pi j}{N} = q$ where $q \in [0, \pi]$ is a continuous variable. So the sum in Eq. (A11) becomes an integral such as

$$D(i = v\tau, \tau) = \frac{e^{-\frac{\bar{\gamma}\tau}{2}}}{\pi} \int_0^\pi dq \times \left\{ \cos\left[2\tau\left(qv - \frac{1}{2}\Delta_q\right)\right] \right.$$
$$\left. - \frac{\bar{\gamma}}{2\Delta_q} \sin\left[2\tau\left(qv - \frac{1}{2}\Delta_q\right)\right] \right\}, \tag{A13}$$

with

$$\Delta_q = \sqrt{2\bar{\kappa}}\sqrt{1 + \eta - \cos(2q)} \tag{A14}$$

where $\eta = \frac{k_0 - (\bar{\gamma}/2)^2}{2\bar{\kappa}}$. The integrand in Eq. (A13) is like a forward-moving wave with angular frequency $\omega(q)$ satisfying the dispersion relation $\omega(q) = \frac{1}{2}\Delta_q$. Then one can define the group velocity (v_g) and butterfly speed (v_b) from there as

$$v_g(q) = \frac{\partial \omega}{\partial q} = \frac{\sqrt{\bar{\kappa}} \sin(2q)}{\sqrt{2[1 + \eta - \cos(2q)]}},$$
$$v_b(\bar{\kappa}, \bar{\gamma}, k_0) = \max_q v_g$$
$$= \sqrt{\bar{\kappa}}\sqrt{1 + \eta - \sqrt{(1+\eta)^2 - 1}}, \tag{A15}$$

where $\max_q v_g = v_g(q^*)$ with q^* satisfying the equation $\cos(2q^*) = (1 + \eta) - \sqrt{(1+\eta)^2 - 1}$. Clearly, at $q = q^*$, $\frac{\partial^2 \omega}{\partial q^2}\big|_{q^*} = 0$ implying that q^* is the saddle point of $\omega(q)$ such that $\frac{\partial^3 \omega}{\partial q^3}\big|_{q^*} < 0$.

Since we have the exact analytical expression of the OTOC for the DC in Eq. (A11), we can directly calculate the VDLE using Eq. (10). This is plotted for two different values of the dissipation in Fig. 23(a) at $\tau = 200$; the corresponding data from simulation are presented in the same plot. The analytical and numerical data exhibit an excellent match. Interestingly, Fig. 23(a) reveals that the greater the dissipation value, the more oscillators tend to achieve enough perturbation to attain $\lambda(v) \approx -\frac{\gamma}{2}$. This, in turn, indicates that the IS is larger for larger γ. This fact is further ensured by the plot of v_b [calculated from Eq. (A15)] as a function of γ presented in Fig. 23(b). There we clearly observe that v_b is an increasing function of γ for the driven dissipative HC. Although this might seem somewhat surprising, actually one has to keep in mind that in Fig. 23, what one measures is how far a perturbation (however small it may be) can reach rather than the magnitude of the perturbation.

Note that in the absence of dissipation ($\bar{\gamma} = 0$) and on-site potential ($k_0 = 0$), we get $\eta = 0$, and the dispersion relation simplifies to $\omega(q) = \sqrt{\bar{\kappa}} \sin(q)$. Consequently, for this conserved harmonically coupled chain, the group velocity is $v_g =$
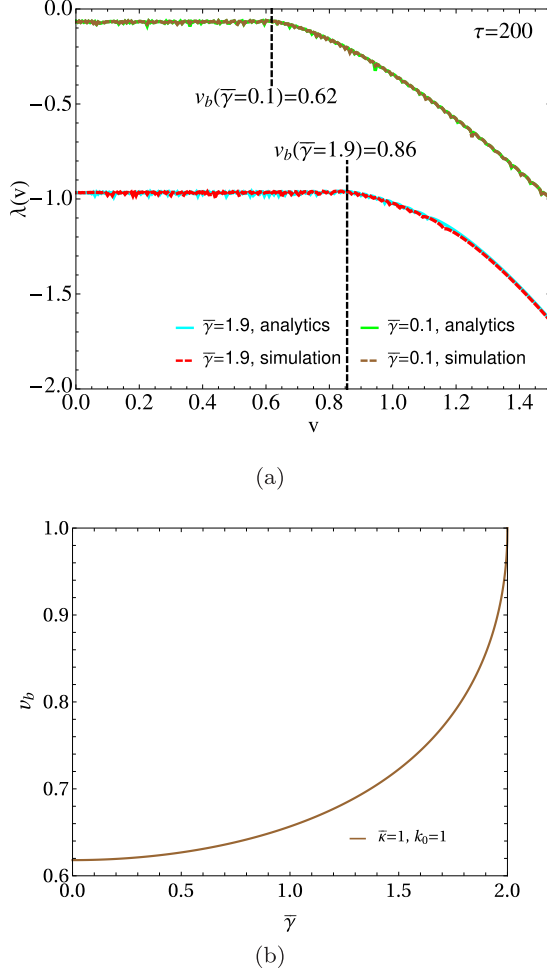
(a)

(b)

FIG. 23. In panel (a) we have plotted VDLE vs v for two different dissipation values, $\bar{\gamma} = 0.1$ and $\bar{\gamma} = 1.9$, both from numerical computation (showed by the solid lines) and analytical calculation from Eq. (A11) (showed by dotted lines) at time $\tau = 200$. We observe that the more the dissipation, the more oscillators gain enough perturbation to reach the VDLE value $\lambda(v) \approx -\frac{\bar{\gamma}}{2}$. This indicates that $v_b(\bar{\gamma})$ is larger for larger dissipation. This is indeed the case, as clearly observed from panel (b), where we have plotted v_b, from Eq. (A15), as a function of $\bar{\gamma}$.

$\sqrt{\bar{\kappa}}\cos(q)$, and the butterfly speed simply becomes $v_b = \sqrt{\bar{\kappa}}$ occurring at $q = q^* = 0$.

Our goal is to analyze the behavior of $D(i, t)$ near $v \approx v_b$. To achieve that, we can do a saddle point approximation of the integral in (A13) by analyzing the integrand near q^*, i.e., letting $q = q^* + \delta q$ where $\delta q \in (-\epsilon, \epsilon)$, ϵ being a very small number. It is important to note that the previous statement is based on the underlying assumption that $q^* \in (0, \pi)$. In other words, the endpoints $q^* = 0$ and $q^* = \pi$ have to be dealt with separately since for them the neighborhoods are restricted only to $\delta q \in (0, \epsilon)$ and $\delta q \in (-\epsilon, 0)$, respectively. In the context of system parameters, the equation $\cos(2q^*) = (1 + \eta) - \sqrt{(1 + \eta)^2 - 1}$ directly implies that $q^* = 0$ and $q^* = \pi$ means $\eta = 0$. An example of a system leading to this scenario is $k_0 = 0 = \gamma$, i.e., the chain of harmonically coupled oscillators in the absence of dissipation and on-site harmonic potential.

The analysis for this case will be done separately at the end of this Appendix. For now, we stick to the general driven dissipative coupled HC for which $\eta \neq 0$. Near $v \approx v_b$, from Eq. (A13), the OTOC becomes

$$D(v\tau \approx v_b\tau, \tau) = \frac{e^{-\frac{\gamma\tau}{2}}}{\pi}\left\{g(q^*)\int_{-\epsilon}^{\epsilon} d(\delta q)\cos[2\tau h(\delta q)]\right.$$
$$\left. + \bar{g}(q^*)\int_{-\epsilon}^{\epsilon} d(\delta q)\sin[2\tau h(\delta q)]\right\}, \quad (A16)$$

where

$$h(\delta q) = (v - v_b)\delta q + \left|\frac{1}{2}\frac{\partial^3 \omega}{\partial q^3}\right|\frac{(\delta q)^3}{3}$$
$$= (v - v_b)\delta q + 2v_b\frac{(\delta q)^3}{3},$$

$$g(q^*, \tau) = \cos\left[2\tau\left(vq^* - \frac{1}{2}\Delta_{q^*}\right)\right]$$
$$- \frac{\bar{\gamma}}{2\Delta_{q^*}}\sin\left[2\tau\left(vq^* - \frac{1}{2}\Delta_{q^*}\right)\right],$$

$$\bar{g}(q^*, \tau) = -\sin\left[2\tau\left(vq^* - \frac{1}{2}\Delta_{q^*}\right)\right]$$
$$- \frac{\bar{\gamma}}{2\Delta_{q^*}}\cos\left[2\tau\left(vq^* - \frac{1}{2}\Delta_{q^*}\right)\right]. \quad (A17)$$

Now, using the fact that $\int_{-a}^{a} dx f(x) = \int_0^a dx[f(x) + f(-x)]$ and $\sin[2\tau h(\delta q)]$ is an odd function, the integral in Eq. (A16) reduces to

$$D(i = v\tau \approx v_b\tau, \tau)$$
$$= \frac{2e^{-\frac{\bar{\gamma}\tau}{2}}}{\pi}g(q^*, \tau)\int_0^{\epsilon} d(\delta q)\cos[2th(\delta q)]$$
$$= \frac{2e^{-\frac{\bar{\gamma}\tau}{2}}g(q^*, \tau)}{\pi}\int_0^{\epsilon} d(\delta q)\cos\left[2(v - v_b)\tau\delta q\right.$$
$$\left. + 4v_b\tau\frac{(\delta q)^3}{3}\right].$$

Now, with the variable transformation

$$(4v_b\tau)^{1/3}\delta q = s \quad \Rightarrow s \in (0, \infty) \text{ as } \tau \to \infty,$$

the above integral becomes

$$D(v\tau \approx v_b\tau, \tau) = \frac{2e^{-\frac{\bar{\gamma}\tau}{2}}g(q^*, \tau)}{(4v_b\tau)^{1/3}\pi}$$
$$\times \int_0^{\infty} ds \cos\left[\frac{s^3}{3} + \frac{2^{\frac{1}{3}}(v - v_b)\tau^{\frac{2}{3}}}{v_b^{\frac{1}{3}}}s\right]. \quad (A18)$$

The above integral is in the form of the well-known Airy integral. So we finally have

$$D(v\tau, \tau) = \begin{cases} \frac{2e^{-\frac{\bar{\gamma}\tau}{2}}g(q^*, \tau)}{(4v_b\tau)^{1/3}}\text{Ai}(z), & \text{for } v \gtrsim v_b \\ \frac{2e^{-\frac{\bar{\gamma}\tau}{2}}g(q^*, \tau)}{(4v_b\tau)^{1/3}}\text{Ai}(-z), & \text{for } v \lesssim v_b \end{cases} \quad (A19)$$

with $z = \frac{2^{\frac{1}{3}}|v_b - v|\tau^{\frac{2}{3}}}{v_b^{\frac{1}{3}}} > 0$. (A20)
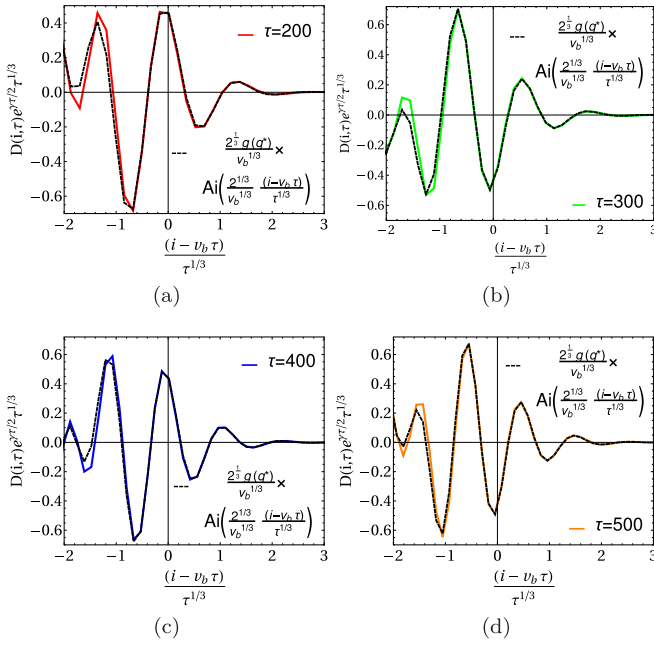
FIG. 24. In the panels we have plotted the exact form of OTOC (scaled by $e^{\gamma \tau/2} \tau^{1/3}$) vs the scaled variable $(i - v_b \tau)/\tau^{1/3}$ from Eq. (A11) for a driven dissipative coupled HC at different τ. We compare these with the corresponding approximate expression of the OTOC obtained in Eq. (A19) using continuum theory. The observation is that at each τ, the exact [shown by solid curve computed from Eq. (A11)] and approximate [shown by dashed curve computed from Eq. (A11)] expressions of the OTOC show perfect agreement near $v \approx v_b$ and start deviating from each other as we go reasonably far from $v \approx v_b$. Parameters used are $\{\bar{\kappa} = 1, k_0 = 0.1, \bar{\gamma} = 0.05\}$.

In order to compare the exact expression of the OTOC in Eq. (A11) with the corresponding approximated expression near $v \approx v_b$ in Eq. (A19), we plot $D(i, \tau)$ (scaled by $\tau^{\frac{1}{3}}$) as a function of $(i - v_b \tau)/\tau^{1/3}$ in Fig. 24 for an arbitrary chosen parameter set $\{\kappa = 1, k_0 = 0.1, \gamma = 0.05\}$. The four panels in Fig. 24 correspond to different τ (sufficiently large). We observe that, for each τ, the exact form of the OTOC (shown by the solid curve) computed from Eq. (A11) exhibits prefect agreement near $v \approx v_b$ with the corresponding approximate form (shown by dashed curve), obtained using a continuum approximation, in Eq. (A19). However, as one moves sufficiently far from $v \approx v_b$ region, the two expressions [Eq. (A11) and Eq. (A19)] start deviating from one other.

Since we are in the limit $\tau \to \infty$, from Eq. (A19), we can use the large z asymptotic of Airy functions, and we have

$$
D(v\tau, \tau) =
\begin{cases}
\frac{\hat{g}(q^*, \tau)}{2\sqrt{\tau}} \, e^{-\frac{\bar{\gamma}}{2}\tau - \frac{2 \cdot 2^{\frac{5}{2}}}{3\sqrt{v_b}} \tau (v-v_b)^{\frac{3}{2}}}, & v > v_b, \\[2ex]
\frac{e^{-\frac{\bar{\gamma}}{2}\tau}}{\sqrt{\tau}} \hat{g}(q^*, \tau) \sin\left[\frac{\pi}{4} + \frac{2^{\frac{5}{2}}\tau}{3\sqrt{v_b}}(v-v_b)^{\frac{3}{2}}\right], & v < v_b,
\end{cases}
$$
$$(A21)$$

where $\hat{g}(q^*, \tau) = \frac{g(q^*)}{2^{-\frac{3}{4}}\sqrt{\pi}(v-v_b)^{\frac{1}{4}} v_b^{\frac{1}{4}}}$. It should be mentioned that, in Eq. (A21), both $\hat{g}(q^*, \tau)$ and v_b are functions of $\bar{\gamma}$ through $q^*(\bar{\gamma})$ and $\eta(\bar{\gamma})$, respectively. So, other than the explicit exponential dependence as $e^{-\frac{\bar{\gamma}}{2}\tau}$, the OTOC depends nontrivially on the dissipation through $\hat{g}(q^*, \tau)$ and v_b. The

velocity-dependent Lyapunov exponent (VDLE), $\lambda(v)$, is defined in Eq. (10). Using this, we obtain that near $v \approx v_b$, the VDLEs are given by

$$
\lambda(v) - \lambda \approx -(v - v_b)^{\frac{3}{2}} \quad \text{for } v > v_b,
$$
$$
\lambda(v) \approx \lambda \quad \text{for } v < v_b, \tag{A22}
$$

where $\lambda = -\frac{\gamma}{2}$.

As stated earlier, we would now like to consider the special case of a harmonically coupled chain without any dissipation and on-site potential (i.e. $k_0 = 0 = \gamma$). For this chain, we have $\eta = \frac{k_0 - (\bar{\gamma}/2)^2}{2\bar{\kappa}} = 0$ leading to $q^* = 0$ or $q^* = \pi$. Without any loss of generality we consider $q^* = 0$ so that now $\delta q \in (0, \epsilon)$ instead of $\delta q \in (-\epsilon, \epsilon)$. Correspondingly, after a saddle point approximation, Eq. (A15) in this case boils down to

$$
D(i = v\tau \approx v_b \tau, \tau) = \frac{1}{\pi} \int_0^\epsilon d(\delta q) \cos[2\tau h(\delta q)], \quad (A23)
$$

where

$$
h(\delta q) = (v - v_b)\delta q + v_b \frac{(\delta q)^3}{6}. \tag{A24}
$$

Note that, for a harmonically coupled chain, $g(q^*, \tau) = 1$ and $\bar{g}(q^*, \tau) = 0$. In the limit $\tau \to \infty$, with the variable transformation $(v_b \tau)^{1/3} \delta q = s$, Eq. (A23) transforms into

$$
D(v\tau \approx v_b \tau, \tau) = \frac{2}{(v_b \tau)^{1/3} \pi}
$$
$$
\times \int_0^\infty ds \cos\left[\frac{s^3}{3} + \frac{2(v - v_b)\tau^{\frac{2}{3}}}{v_b^{\frac{1}{3}}} s\right]. \quad (A25)
$$

As already discussed, the integral in Eq. (A25) is in the well-known form of the Airy function, and we have

$$
D(v\tau, \tau) =
\begin{cases}
\frac{2}{(v_b \tau)^{1/3}} \text{Ai}(z), & \text{for } v \gtrsim v_b \\[1ex]
\frac{2}{(v_b \tau)^{1/3}} \text{Ai}(-z), & \text{for } v \lesssim v_b
\end{cases} \quad (A26)
$$
$$
\text{with} \quad z = \frac{2|v_b - v|\tau^{\frac{2}{3}}}{v_b^{\frac{1}{3}}} > 0. \tag{A27}
$$

Note the difference between the expressions of the OTOC for the driven dissipative coupled HC in Eq. (A19) and (A20) with that of a harmonically coupled chain in Eq. (A26) and (A27). Due to the absence of the time-dependent term $g(q^*, \tau)$ in Eq. (A26), we expect collapse of data at different τ when the OTOC $D(i, \tau)$ is scaled by $\tau^{\frac{1}{3}}$. This is indeed observed in Fig. 25 where the exact expression for OTOC (scaled by $\tau^{\frac{1}{3}}$) in Eq. (A11) for a harmonically coupled chain (with $\kappa = 1$) is plotted against the scaled variable $(i - v_b \tau)/\tau^{1/3}$. Apart from the excellent data collapse at different τ (shown by the solid curves), Fig. 25 exhibits perfect agreement with the exact OTOC expression in Eq. (A11) with the corresponding approximated expression (obtained through continuum theory and saddle point approximation) in a considerably large range around $v \approx v_b$ in Eq. (A19) (shown by the dashed curve).
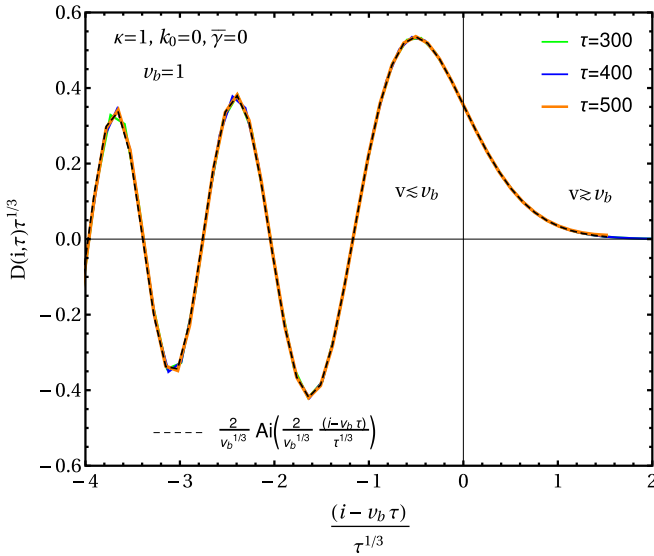
FIG. 25. Here we compare the exact expression of the OTOC in Eq. (A11) for a harmonically coupled DC (in the absence of dissipation and on-site harmonic potential) to the approximate expression of the OTOC in Eq. (A19) near $v \approx v_b$ obtained using continuum theory. The OTOC (scaled by a factor $\tau^{1/3}$) at different times [shown by the solid curves computed from Eq. (A11)] collapse perfectly on top of each other when plotted against the scaled variable $(i - v_b \tau)/\tau^{1/3}$. This data collapse also exhibits perfect agreement with the corresponding continuum approximation [the dashed curve computed from Eq. (A19)] within a reasonably large range about $v \approx v_b$. Parameters used are $\{\bar{\kappa} = 1, k_0 = 0, \bar{\gamma} = 0\}$.

APPENDIX B: COMPARING UNCOUPLED AND COUPLED DUFFING OSCILLATORS IN DIFFERENT DYNAMICAL REGIMES

Here we present a brief comparison between the dynamical behaviors of uncoupled and coupled Duffing oscillators in the sustained chaos, transient chaos, and nonchaotic regimes. To do so, we have plotted the corresponding finite-time Lyapunov exponents in Fig. 26.

In the sustained chaos regime, we observe that depending on the system parameters, the uncoupled and coupled Duffing oscillators can behave similarly or they can behave in a completely different manner. More elaborately, in Fig. 26(a) we observe that the uncoupled Duffing oscillator can be as chaotic
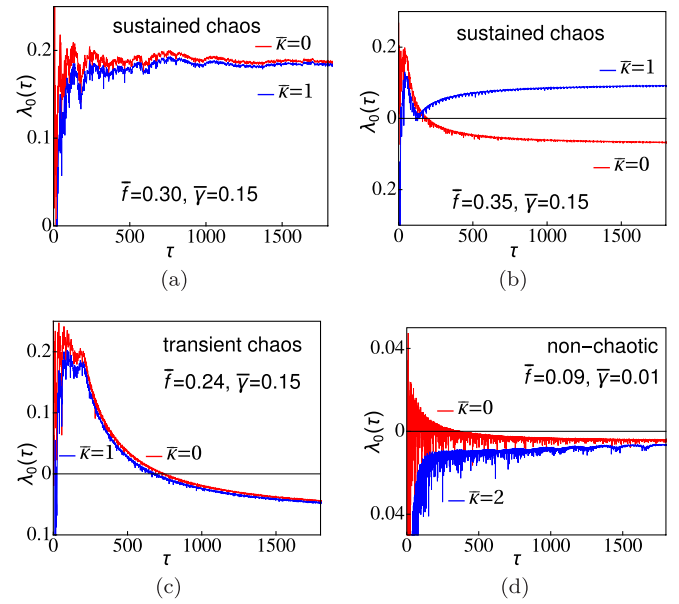

FIG. 26. This figure shows comparison among different dynamical behaviours of coupled ($\kappa \neq 0$) and uncoupled ($\kappa = 0$) Duffing oscillators.

as the coupled oscillator with both having positive Lyapunov exponents. In sharp contrast, Fig. 26(b) interestingly exhibits that, with a moderate variation of the driving amplitude, the coupled Duffing oscillator remains chaotic ($\lambda > 0$) whereas the uncoupled one becomes nonchaotic ($\lambda < 0$).

For the case of transient chaos, as shown in Fig. 26(c), both the uncoupled and coupled oscillators are chaotic at small time and nonchaotic at large time. The only difference is that the time at which the FTLE crosses Lyapunov zero [$\lambda_0(\tau) = 0$] is smaller for the coupled oscillator with respect to the uncoupled one. In Fig. 26(d) the coupled and uncoupled Duffing oscillators both exhibit nonchaotic behaviors at large time. However, notably here, the uncoupled oscillator has $\lambda_0(\tau) > 0$ at small τ in contrast to the coupled one, which remains nonchaotic at all time.

In a nutshell, we conclude that the role of coupling can be most prominent in the sustained chaos regime, whereas the difference between the behaviors of the uncoupled and coupled Duffing oscillators is comparatively small in the other dynamical regimes.

[1] E. Lorenz, *The Essence of Chaos* (University of Washington Press, Seattle, 1993).

[2] S. H. Strogatz, *Nonlinear Dynamics and Chaos* (Perseus Books, Reading, MA, 1994).

[3] M. C. Gutzwiller, *Chaos in Classical and Quantum Mechanics* (Springer-Verlag, New York, 1990).

[4] F. Haake, *Quantum Signatures of Chaos* (Springer-Verlag, Berlin, 1991).

[5] X. Zeng, R. A. Pielke, and R. Eykholt, Bull. Am. Meteorol. Soc. **74**, 631 (1993).

[6] A. M. Selvam, J. Adv. Math. Appl. **1**, 181 (2012).

[7] A. Huppert and L. Stone, Am. Nat. **152**, 447 (1998).

[8] R. J. Field and L. Györgyi, editors, *Chaos in Chemistry and Biochemistry*, (World Scientific, Singapore, 1993).

[9] P. Gaspard, Phys. A **263**, 315 (1999).

[10] P. Gaspard, M. E. Briggs, M. K. Francis, J V. Sengers, R. W. Gammon, J. R. Dorfman, and R. V. Calabrese, Nature (London) **394**, 865 (1998).

[11] R. Srivastava, P. K. Srivastava, and J. Chattopadhyay, Eur. Phys. J. Special Topics **222**, 777 (2013).

[12] J. E. Skinner, Nature Bio/Technol. **12**, 596 (1994).

[13] W. L. Ditto, AIP Conf. Proc. **376**, 175 (1996).

[14] A. Lesne, Biology Forum/Rivista di Biologia **99**, 467 (2006).

[15] A. L. Lloyd and D. Lloyd, Biol. Rhythm Res. **26**, 233 (1995).

[16] A. S. Tchana, P. Woafo, and R. Yamapi, Int. J. Bifurcation Chaos **18**, 3473 (2008).

[17] C. A. K. Kwuimy and P. Woafo, Nonlinear Dyn. **53**, 201 (2008).

[18] B. Bao, Z. Ma, J. Xu, Z. Liu, and Q. Xu, Int. J. Bifurcation Chaos **21**, 2629 (2011).

[19] K. T. Chau and Z. Wang, *Chaos in Electric Drive Systems* (John Wiley & Sons (Asia), Singapore, 2011).

[20] J. G. Wei and G. Leng, Appl. Math. Comput. **88**, 77 (1997).

[21] J. Kozlowski, U. Parlitz, and W. Lauterborn, Phys. Rev. E **51**, 1861 (1995).

[22] J. A. Vastano and H. L. Swinney, Phys. Rev. Lett. **60**, 1773 (1988).

[23] A. Wacker, S. Bose, and E. Schöll, Europhys. Lett. **31**, 257 (1995).

[24] S. Lepri, A. Politi, and A. Torcini, J. Stat. Phys. **82**, 1429 (1996).

[25] S. Lepri, A. Politi, and A. Torcini, J. Stat. Phys. **88**, 31 (1997).

[26] G. Giacomelli, R. Hegger, A. Politi, and M. Vassalli, Phys. Rev. Lett. **85**, 3616 (2000).

[27] D. Pazo, J. M. Lopez, and A. Politi, Phys. Rev. Lett. **117**, 034101 (2016).

[28] R. Livi, A. Politi, S. Ruffo, and A. Vulpiani, J. Stat. Phys. **46**, 147 (1987).

[29] H. Kantz and P. Grassberger, J. Phys. A: Math. Gen. **21**, L127 (1988).

[30] A. Lakshminarayan and S. Tomsovic, Phys. Rev. E **84**, 016218 (2011).

[31] R. van Zon, H. van Beijeren, and C. Dellago, Phys. Rev. Lett. **80**, 2035 (1998).

[32] P. Gaspard, Prog. Theor. Phys., Suppl. **150**, 64 (2003).

[33] D. Stahlke and R. Wackerbauer, Phys. Rev. E **83**, 046204 (2011).

[34] N. Chopra and M. W. Spong, IEEE Trans. Autom. Control **54**, 353 (2009).

[35] P. K. Mohanty, Phys. Rev. E **70**, 045202(R) (2004).

[36] P. K. Mohanty and A. Politi, J. Phys. A: Math. Gen. **39**, L415 (2006).

[37] A. Das, S. Chakrabarty, A. Dhar, A. Kundu, D. A. Huse, R. Moessner, S. S. Ray, and S. Bhattacharjee, Phys. Rev. Lett. **121**, 024101 (2018).

[38] V. Khemani, D. A. Huse, and A. Nahum, Phys. Rev. B **98**, 144304 (2018).

[39] D. Kumar, S. Bhattacharjee, and S. S. Ray, arXiv:1906.00016 (2019).

[40] T. Bilitewski, S. Bhattacharjee, and R. Moessner, Phys. Rev. Lett. **121**, 250602 (2018).

[41] Y. Sekino and L. Susskind, J. High Energy Phys. 10 (2008) 065.

[42] S. H. Shenker and D. Stanford, J. High Energy Phys. 03 (2014) 067.

[43] E. B. Rozenbaum, S. Ganeshan, and V. Galitski, Phys. Rev. Lett. **118**, 086801 (2017).

[44] I. Kukuljan, S. Grozdanov, and T. Prosen, Phys. Rev. B **96**, 060301(R) (2017).

[45] A. Bohrdt, C. Mendl, M. Endres, and M. Knap, New J. Phys. **19**, 063001 (2017).

[46] A. Lakshminarayan, Phys. Rev. E **99**, 012201 (2019).

[47] Y. L. Zhang, Y. Huang, and X. Chen, Phys. Rev. B **99**, 014303 (2019).

[48] B. Chakrabarty, S. Chaudhuri, and R. Loganayagam, J. High Energy Phys. 07 (2019) 102.

[49] R.-Q. He and Z.-Y. Lu, Phys. Rev. B **95**, 054201 (2017).

[50] R. Fan, P. Zhang, H. Shen, and H. Zhai, Sci. Bull. **62**, 707 (2017).

[51] Y. Huang, Y.-L. Zhang, and X. Chen, Ann. Phys. (Berlin) **529**, 1600318 (2017).

[52] S. Ray, S. Sinha, and K. Sengupta, Phys. Rev. A **98**, 053631 (2018).

[53] J. Polchinski and V. Rosenhaus, J. High Energy Phys. 04 (2016) 1.

[54] J. Maldacena and D. Stanford, Phys. Rev. D **94**, 106002 (2016).

[55] C.-J. Lin and O. I. Motrunich, Phys. Rev. B **97**, 144304 (2018).

[56] S. Gopalakrishnan, Phys. Rev. B **98**, 060302(R) (2018).

[57] M. McGinley, A. Nunnenkamp, and J. Knolle, Phys. Rev. Lett. **122**, 020603 (2019).

[58] X. Chen and T. Zhou, Phys. Rev. B **100**, 064305 (2019).

[59] G. Duffing, *Erzwungene Schwingungen bei veränderlicher Eigenfrequenz und ihretechnische Bedeutung* (F. Vieweg & Sohn, Braunschweig, 1918).

[60] Y. Ueda, Int. J. Non-linear Mech. **20**, 481 (1985).

[61] Y. Ueda, J. Stat. Phys. **20**, 181 (1979).

[62] Y. Ueda, Chaos, Solitons Fractals **1**, 199 (1991).

[63] W. Szemplinska-Stupnicka, J. Sound Vib. **113**, 155 (1987).

[64] V. Englisch and W. Lauterborn, Phys. Rev. A **44**, 916 (1991).

[65] I. Kovacic and M. J. Brennan (Eds.), *The Duffing Equation* (John Wiley & Sons, Chichester, United Kingdom, 2011).

[66] J. A. Gottwald, L. N. Virgin, and E. H. Dowell, J. Sound Vib. **158**, 447 (1992).

[67] R. Chabreyrie and N. Aubry, arXiv:1108.4118 (2011).

[68] A. Kenfack, Chaos Solitons Fractals **15**, 205 (2003).

[69] D. E. Musielak, Z. E. Musielak, and J. W. Benner, Chaos Solitons Fractals **24**, 907 (2005).

[70] R. Jothimurugan, K. Thamilmaran, S. Rajasekar, and M. A. F. Sanjuan, Nonlinear Dyn. **83**, 1803 (2016).

[71] X. Wei, M. F. Randrianadrasana, M. Ward, and D. Lowe, Math. Probl. Eng. **2011**, 248328 (2011).

[72] T. Kapitaniak, Phys. Rev. E **47**, R2975(R) (1993).

[73] Y.-C. Lai and R. L. Winslow, Physica D **74**, 353 (1994).

[74] M. G. Clerc, S. Coulibaly, M. A. Ferré, and R. G. Rojas, Chaos **28**, 083126 (2018).

[75] M. Zapateiro, Y. Vidal, and L. Acho, IFAC Proc. **46**, 749 (2013).

[76] K. Murali and M. Lakshmanan, Phys. Rev. E **48**, R1624 (1993).

[77] N. Q. Hu and X. S. Wen, J. Sound Vib. **268**, 917 (2003).

[78] Y. Zhang, H. Mao, H. Mao, and Z. Huang, Results Phys. **7**, 3243 (2017).

[79] Xuanchao Liu and Xiaolong Liu, J. Comput. **6**, 359 (2011).

[80] D. K. Umberger, C. Grebogi, E. Ott, and B. Afeyan, Phys. Rev. A **39**, 4835 (1989).

[81] G. Benettin, L. Galgani, A. Giorgilli, and J. M. Strelcyn, Meccanica **15**, 21 (1980).

[82] E. H. Lieb and D. W. Robinson, Commun. Math. Phys. **28**, 251 (1972).

[83] R. J. Deissler, Phys. Lett. A **100**, 451 (1984).

[84] K. Kaneko, Physica D **23**, 436 (1986).

[85] R. J. Deissler and K. Kaneko, Phys. Lett. A **119**, 397 (1987).

[86] J. H. Peng, E. J. Ding, M. Ding, and W. Yang, Phys. Rev. Lett. **76**, 904 (1996).

[87] M. Lakshmanan and K. Murali, *Chaos in Nonlinear Oscillators* (World Scientific, Singapore, 1996).

[88] J. N. Blakely and D. J. Gauthier, Int. J. Bifurcation Chaos **10**, 835 (2000).

[89] V. G. Ivancevic and T. T. Ivancevic, *High Dimensional Chaotic and Attractor Systems* (Springer-Verlag, Dordrecht, 2007).

[90] Z. E. Musielak and D. E. Musielak, Int. J. Bifurcation Chaos **19**, 2823 (2009).

[91] A. Roy and J. K. Bhattacharjee, Phys. Lett. A **288**, 1 (2001).

[92] B. Pokharel, M. Z. R. Misplon, W. Lynn, P. Duggins, K. Hallman, D. Anderson, A. Kapulkin, and A. K. Pattanayak, Sci. Rep. **8**, 2108 (2018).